Longitudinal Spin Diffusion of a Two-Domain Ultracold Non-Degenerate Bose Gas

by

Lindsay Elizabeth Babcock

B.Sc., University of Waterloo, 2019

Thesis Submitted in Partial Fulfillment of the
Requirements for the Degree of
Master of Science

in the
Department of Physics
Faculty of Science

SIMON FRASER UNIVERSITY
Spring 2022

Declaration of Committee

Name:	**Lindsay Elizabeth Babcock**
Degree:	**Master of Science**
Thesis title:	**Longitudinal Spin Diffusion of a Two-Domain Ultracold Non-Degenerate Bose Gas**
Committee:	**Chair:** Malcolm Kennett Associate Professor, Physics
	Jeffrey McGuirk Supervisor Associate Professor, Physics
	Paul Haljan Committee Member Associate Professor, Physics
	Kero Lau Examiner Assistant Professor, Physics

Abstract

This thesis explores the effects of domain wall width on a two-domain ultracold non-degenerate trapped gas of Rubidium-87. A gas of Rubidium-87 atoms is evaporatively cooled to just above quantum degeneracy. Atoms are then prepared in a configuration of two longitudinal spin domains separated by a coherent helical domain wall, and spin diffusion is observed. We demonstrate the slowing of spin wave oscillations as domain wall width is increased, as a result of increased coherent spin interactions. In the presence of a linear potential gradient, spin domains are stabilized and reach a maximum lifetime near the equilibrium domain wall width. Equilibrium domain wall widths are determined through analysis of the domain wall width relaxation rate and results show reasonably good agreement with hydrodynamic approximations of the quantum Boltzmann equation.

Keywords: ultracold atoms, spin diffusion

Acknowledgements

I would like to respectfully acknowledge that the SFU Burnaby campus is located on the unceded traditional territories of the Coast Salish peoples, including the Tsleil-Waututh, Kwikwetlem, Squamish and Musqueam Nations.

I am sincerely grateful to have had the opportunity to be supervised by Dr. Jeffrey McGuirk. Jeff's guidance and patience over the last few years has been invaluable. I enjoyed the freedom I was given to learn and explore science on my own, while always knowing he would be happy to provide feedback and ideas when asked. None of this work would have been possible without his knowledge and support, for that I cannot thank him enough.

I must thank the members of the McGuirk group for the work they have done in collecting data and maintaining the experimental apparatus used in this thesis. A very special thanks to Olha Farion for delightful atomic physics discussions and for bringing so much kindness and joy into the lab everyday. I must also thank Sean Graham for teaching me so much about the experimental apparatus. Our time in the lab only overlapped shortly, but the knowledge I gained from him was extremely helpful.

I am grateful for the entire SFU Physics community for providing such a positive environment for learning, even virtually in the face of a pandemic. A special thanks to Matt Martin, Jon Barenboim, and all of the other students that joined our little group over the years. All of the coffee breaks, hikes, brewery outings, and games nights really helped to make my time at SFU enjoyable. Also, my thanks to many of the experienced graduate students that welcomed me to SFU, especially Brendin Chow and Alex Kurkjian, who were great friends and always provided me with helpful advice on navigating grad school.

To Palma-Rosita Colalancia, Claire Leuty, Natalie Hart-Dixon, and Lara Jeftic, whose friendships have withstood the test of time and distance. I am so grateful for all of their love, support, and their endless patience in listening to me complain about physics. I must also express my appreciation for my best feline friend, Goob, who never left my side during the long days of thesis writing.

Finally, to my Dad for instilling a love of science in me at a young age, to my Mom, who convinced me that I was capable of anything I set my mind to and who worked so hard to give me all of the opportunities she never had, and to my sister who has constantly cheered me on. Thank you, I would not be where I am today without all of you.

Table of Contents

List of Figures

Chapter 1

Introduction

Since the idea of a fundamental limit on temperature, known as absolute zero, was introduced, scientists have been working to reach colder temperatures to explore novel physics. In the late 1900s huge advancements in low-temperature physics stemmed from metrology, specifically with the goal of advancing the accuracy of atomic clocks [1]. In atomic clocks, cold atoms are incredibly valuable as their low velocities allow for more precise measurements. These studies led experimentalists to the development of laser cooling and trapping techniques in the 1970s. Steven Chu, Claude Cohen-Tannoudji, and William D. Phillips were awarded the 1997 physics Nobel prize for these discoveries [2, 3].

Building off of this work, in 1995, Carl Wieman and Eric Cornell were able to cool a dilute gas of Rubidium-87 down to 170 nK, creating the first ever gaseous Bose-Einstein condensate (BEC) [4]. This was followed only months later by Wolfgang Ketterle making the first Sodium BEC [5]. All three were awarded the 2001 Nobel prize for this groundbreaking achievement. Bose-Einstein condensation is a remarkable phase transition taking place at ultracold temperatures in an ensemble of bosons. As atoms cool, their thermal de Broglie wavelength, which characterizes the spatial extent of their wavefunction, gets larger. When this value becomes larger than distances between atoms in an ensemble, the wavefunctions begin to overlap, and quantum statistics are required to describe the system. For an ensemble of bosons, atoms obey Bose-Einstein statistics, which predicts all atoms in the ensemble will occupy the same quantum ground state when their temperature is below some critical temperature. This phenomena was originally theorized by Bose and Einstein in 1924 [6, 7].

The new techniques for trapping and cooling atoms to create BECs, as well as the BECs themselves, sparked a field of research into ultracold atoms and even offer applications into other fields such as condensed matter physics [8, 9] and quantum information [10, 11]. Low temperatures provide an ideal environment for studying quantum mechanical effects, and the high tunability of ultracold atomic systems allows for of a wide range of parameters to be easily explored. A particularly interesting area of study in the field of ultracold atoms is out-of-equilibrium spinor gases. Specifically, this thesis will focus on the diffusion of an out-of-equilibrium Rb-87 spinor gas, with temperatures just above the critical temperature. In the regime we are exploring, the atomic gas sample is non-degenerate, but exhibits quantum mechanical behaviours.

Previous experimental studies of non-degenerate ultracold spin gases have shown collective behaviour of spins during diffusion, for example spin waves, where an atomic cloud exhibits a spatio-temporal oscillation of spin [12, 13]. Spin waves are a result of the identical spin rotation effect, which arises due to quantum indistinguishability during binary collisions [14, 15]. The spin rotation effect helps to preserve local spin orientation and can significantly slow spin diffusion. The McGuirk group has done significant research into understanding and controlling spin-wave dynamics. They have investigated the effects of coherence between longitudinal spin domains on spin diffusion of a two-domain ultracold gas of Rubidium-87 above degeneracy [16]. They have also demonstrated the ability to alter spin diffusion in these systems through the use of a spin-dependent potential to speed, slow, or completely stop spin wave oscillations [17]. This thesis builds on this previous work to explore the role of domain wall width on spin-wave dynamics. Results from this work may be useful in many quantum technologies that require precise control and transport of atomic spins, such as spintronics devices [18].

This thesis is organized as follows. Chapter 2 reviews the energy level structure of Rubidium-87 and Zeeman splitting of its hyperfine states. Next, the two-level quantum system, including the Bloch sphere representation is reviewed. An overview of spin-dynamics theory is given, including a description of the identical spin rotation effect that modifies spin dynamics in ultracold atomic systems just above degeneracy. Finally, the quantum Boltzmann equation is presented. This equation describes the expected spin-dynamics of an atomic gas, including the effects of the identical spin rotation effect and applied differential potentials.

Chapter 3 describes the experimental system used to prepare and measure an ultracold gas of Rb-87 atoms. We discuss a method of preparing the sample gas, including trapping and evaporatively cooling atoms. Techniques for preparing spin states in arbitrary configurations, as well as imaging and longitudinal spin measurement procedures, are presented.

The methods of controlling differential potentials are discussed in Chapter 4. First, a description of Ramsey interferometry as a technique for measuring transition frequencies is given. We present methods of creating various differential potentials and methods of correcting inhomogeneties within a potential.

Chapter 5 explores the effects of domain wall width on longitudinal spin diffusion. Experimental and simulated results are analyzed to describe the dynamics of two-domain spin gases over a wide range of domain wall widths. Dynamics are discussed in both uniform differential potential and in a positive linear potential gradient. In Section 5.2.1 It is shown that in a uniform potential, spin-wave oscillations and damping rates are decreased in atomic clouds with larger domain walls. The results are explained in terms of the identical spin rotation effect. Section 5.2.2 shows the results of varying domain wall width on spin-wave dynamics in the presence of a spin-dependent potential. In a positive linear differential potential the spin waves show significantly different behaviour than in a uniform differential potential, as domains are stabilized against longitudinal spin-waves. We observe a maximum spin lifetime at an equilibrium domain wall width, where transients are minimized. To further understand spin diffusion in a spin-dependent potential, Section 5.3 studies the relaxation of domain wall widths. The relationship between equilibrium domain wall widths and differential potential gradient size is examined. Results are compared to analytic approximations of the quantum Boltzmann equation in the hydrodynamic limit.

Results are summarized in Chapter 6. Suggestions for future spin diffusion experiments are given.

Chapter 2

Spin Dynamics Theory

The following Chapter aims to provide a brief summary of the theory behind spin dynamics in an ultracold Rubidium-87 atomic gas. First, the fine and hyperfine structure of Rb-87 is described. Next, the two-level quantum system is reviewed. The identical spin rotation effect, which drives spin dynamics, is then discussed. Finally, the mathematical description governing spin dynamics of a nonequilibrium quantum gas, the quantum Boltzmann equation, is presented.

2.1 Rubidium-87

2.1.1 Energy Level Structure

Rubidium-87 is a long-lived isotope of Rubidium. It contains 37 electrons, with only one in its outermost shell, giving a $5S$ electron configuration. Spin-orbit interactions and relativistic energy corrections give rise to a fine structure doublet, splitting the first excited state, $5P$, into two states, $5P_{1/2}$ and $5P_{3/2}$. The quantum number classifying the fine structure is the total angular momentum, $\vec{J}$, given by

$$\vec{J} = \vec{L} + \vec{S}, \tag{2.1}$$

where $\vec{L}$ is the electron orbital angular momentum and $\vec{S}$ is the electron spin. The transition $5S_{1/2} \rightarrow 5P_{1/2}$ is known as the D_1 line, while the $5S_{1/2} \rightarrow 5P_{3/2}$ transition is the D_2 line. Work done in this thesis focuses only on the $5S_{1/2}$ and $5P_{3/2}$ states.

Energy levels are further split into hyperfine states arising from the coupling of the nuclear magnetic moment to the electron's angular momentum. The total angular momentum of a hyperfine state is

$$\vec{F} = \vec{J} + \vec{I}, \tag{2.2}$$

where $\vec{I}$ is the total nuclear angular momentum, which is 3/2 for Rb-87. Figure 2.1 shows the fine and hyperfine structure of Rb-87.

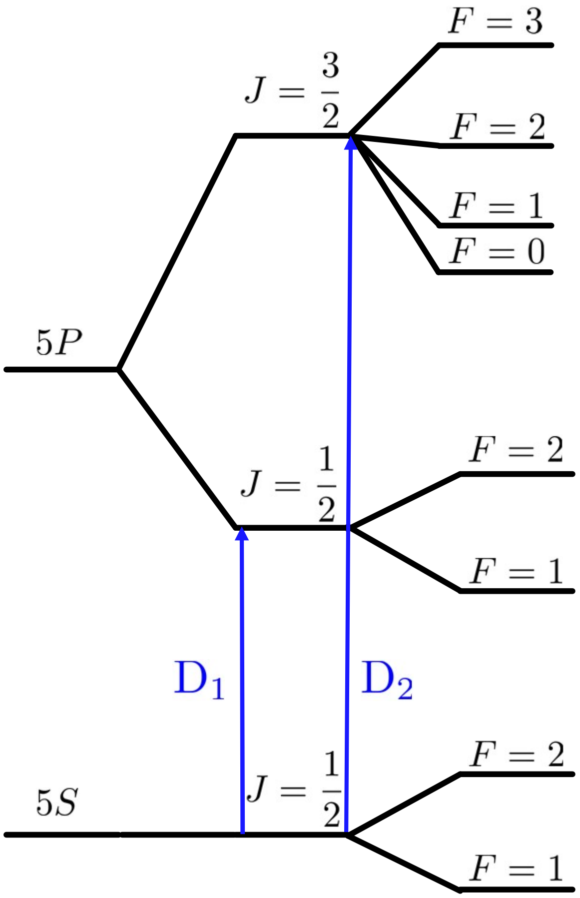

Figure 2.1: Fine and hyperfine structure of of Rb-87 $5S$ and $5P$ states. Energy splittings are not to scale

2.1.2 Zeeman Effect

In the presence of a magnetic field each hyperfine state is further split into $2F+1$ Zeeman sub-levels, categorized by quantum number $m_F = -F, -F+1, ..., F-1, F$. The Hamiltonian describing the atomic magnetic moment coupling to a magnetic field, $\vec{B}$, is [19]

$$H_{\text{mag}} = (\mu_B g_J \vec{J} + \mu_N g_I \vec{I}) \cdot \vec{B}, \tag{2.3}$$

where μ_B and μ_N are the Bohr and nuclear magnetons, and g_J and g_I are the Landé and nuclear g-factors.

In the low to intermediate field regime where $\mu_B B$ is of similar order to the hyperfine splitting (ΔE_{HF}) the Zeeman energy splitting is given by the Breit-Rabi formula [20, 21],

$$\Delta E = \frac{-\Delta E_{HF}}{2(2I+1)} - \mu_B g_I m_F B \pm \frac{\Delta E_{HF}}{2}\sqrt{1 + \frac{4m_F x}{2I+1} + x^2}, \tag{2.4}$$

where

$$x = (g_I + g_J)\frac{\mu_B B}{\Delta E_{hf}}. \tag{2.5}$$

The Breit-Rabi formula is only valid for states with $J = 1/2$. Figure 2.2 shows the splitting of Rb-87 $5S_{1/2}$ levels in the presence of a magnetic field.

In weak magnetic fields the states $|F = 1, m_F = -1\rangle$ and $|F = 2, m_F = 1\rangle$ are trappable. These states have almost identical magnetic moments, leading to approximately the same first-order Zeeman shift. Further, at a certain magnetic field they have identical second-order Zeeman shift. This renders their transition frequency insensitive to fluctuations in magnetic field. These states comprise a pseudo-spin-1/2 doublet, which will be discussed further in Section 2.2.

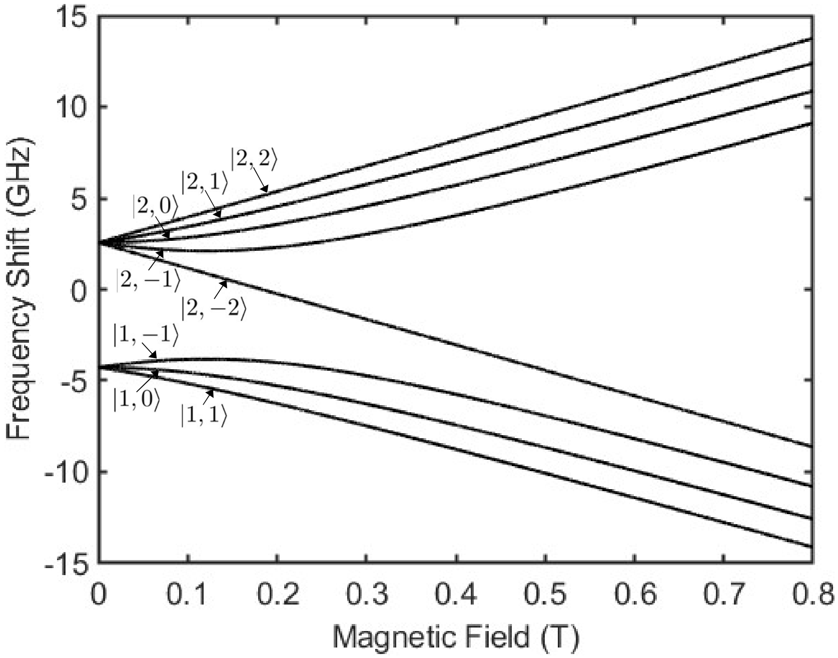

Figure 2.2: Zeeman shift of the $5S_{1/2}$ state of Rb-87. Labelled kets are of the form $|F, m_F\rangle$.

2.2 Two-level Quantum Systems

2.2.1 Rabi Oscillations

Any two-level quantum system can be analogously described as spin-1/2 doublet. The pseudo-spin-1/2 system studied in this thesis is comprised of the $|F = 1, m_F = -1\rangle$ and $|F = 2, m_F = 1\rangle$ hyperfine ground-states of Rb-87, which we will further refer to as $|1\rangle$ and $|2\rangle$ respectively. The lower energy state, $|1\rangle$, is taken as the ground state, while the higher energy $|2\rangle$ is the excited state in the spin-1/2 description. When placed in an electromagnetic field this system can be described by the Hamiltonian

$$H = \hbar \begin{pmatrix} -\frac{\omega_0}{2} & \Omega_R e^{\frac{i\omega t}{2}} \\ \Omega_R e^{\frac{-i\omega t}{2}} & \frac{\omega_0}{2} \end{pmatrix}, \tag{2.6}$$

where ω_0 is the frequency splitting between the two states, ω is the frequency of the electromagnetic field, and Ω_R is the Rabi frequency which describes the coupling strength between the atom and field. In this Hamiltonian the rotating wave approximation, which ignores fast oscillating terms, has been applied.

The time-dependent Schrodinger equation for this Hamiltonian can then be solved. For an atom initially in the ground state, the probability of finding it in the excited state after continuously interacting with an electomagnetic field for time t is given by [22]

$$P_2(t) = \left(\frac{\Omega_R}{\Omega'_R}\right)^2 \sin^2\left(\frac{\Omega'_R t}{2}\right). \tag{2.7}$$

$\Omega'_R = \sqrt{\Omega_R^2 + \delta^2}$ is the effective Rabi frequency, and $\delta = \omega - \omega_0$ is the electromagnetic field's detuning from the $|1\rangle \to |2\rangle$ transition frequency. The probability of finding the atom in an excited state is maximized for a π-pulse, where $\Omega'_R t_\pi = \pi$. As the detuning from resonance increases, the probabilty amplitude decreases and the oscillation frequency increases.

2.2.2 Bloch Sphere Representation

It is often convenient to visualize two-level quantum systems in terms of the Bloch sphere picture. The Bloch sphere is shown in Figure 2.3, where the position of the Bloch vector within the sphere describes the quantum state. A general quantum state is given by

$$|\Psi\rangle = \cos\left(\frac{\theta}{2}\right)|2\rangle + e^{i\phi}\sin\left(\frac{\theta}{2}\right)|1\rangle, \tag{2.8}$$

where θ is the polar angle ($0 \leq \theta \leq \pi$) and ϕ is the azimuthal angle ($0 \leq \phi \leq 2\pi$). On the Bloch sphere, the longitudinal spin is represented by the Bloch vector's projection along the $\hat{z}$-axis, with the ground and excited states on opposite ends of the sphere. The transverse spin is described in the $\hat{x} - \hat{y}$ plane. A Bloch vector along the $\hat{x} - \hat{y}$ plane represents an equal superposition of states with some phase ϕ. Note that the $\hat{x} - \hat{y} - \hat{z}$ coordinate system here refers to spin space, rather than real space.

The evolution of a state due to interaction with an electromagnetic field can be thought of as the state vector precessing around a torque vector, $\vec{\Omega} = (\Omega_R, 0, \delta)$. In a reference frame rotating at frequency ω, the evolution is described by [23]

$$\frac{\mathrm{d}\vec{\Psi}}{\mathrm{d}t} = \vec{\Omega} \times \vec{\Psi}. \tag{2.9}$$

Figure 2.4 shows the rotation of the Bloch vector in two different scenerios. When the electromagnetic field is on resonance with the atomic transition ($\delta = 0$), the torque vector

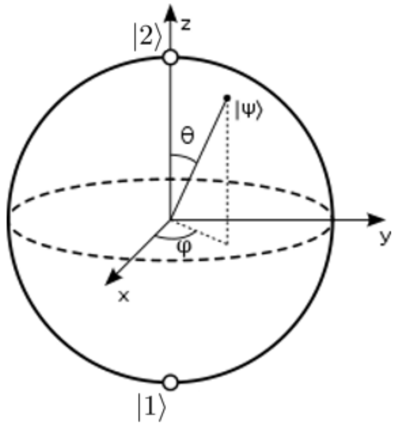

Figure 2.3: A Bloch sphere representation of a two-level quantum system. The north pole of the sphere corresponds to the $|2\rangle$ state and the south pole corresponds to the $|1\rangle$ state.The Bloch vector $|\Psi\rangle$ represents the quantum state and is described by the angles θ and ϕ.

lies along the $\hat{x}$-axis and the Bloch vector precesses between states $|1\rangle$ and $|2\rangle$. For a field with some detuning from the atomic transition ($\delta \neq 0$), the torque vector lies closer to one of the poles, depending on the sign of the detuning, and the Bloch vector precesses more quickly around it, staying closer to the pole.

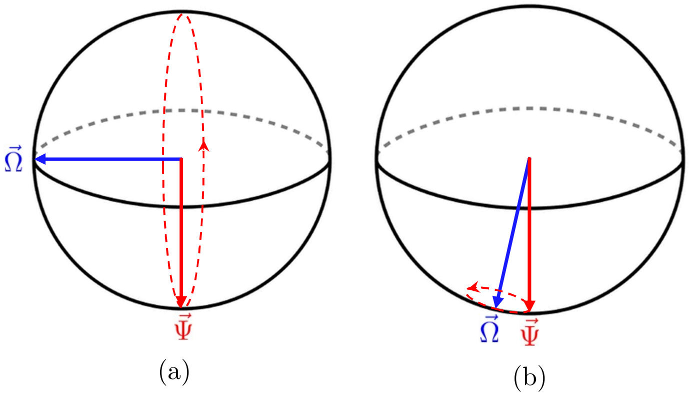

(a)

(b)

Figure 2.4: Bloch vector rotation around the torque vector. a) For $\delta = 0$, the Bloch vector rotates between states $|1\rangle$ and $|2\rangle$. b) For $\delta \neq 0$, the Bloch vectors rotates around the torque vector closer to one of the poles.

2.3 Spin Dynamics

The previous Sections have described the theory of individual spins; however, to understand spin dynamics we must now expand this discussion to the interactions of many spins within an ultracold atomic gas.

2.3.1 Identical Spin Rotation Effect

The identical spin rotation effect (ISRE) is a quantum mechanical effect that leads to spin exchange during atomic collisions. The ISRE has been shown to give rise to surprising macroscopic collective behaviour in non-degenerate ultracold spin-polarized gases, leading to spatio-temporal spin oscillations or "spin waves" [14]. A similar effect, known as the Leggett-Rice effect, has been shown to drive spin waves in strongly interacting gases and liquids [24].

In ultracold systems above degeneracy the ISRE arises when the thermal de Broglie wavelength,

$$\lambda_{\mathrm{dB}} = \sqrt{\frac{2\pi\hbar^2}{mk_{\mathrm{B}}T}}, \tag{2.10}$$

becomes larger than the relevant collision lengths of a system, leading to a spatial overlap of atomic wavefunctions during interactions. For collisions between atoms with non-orthogonal spin states, the overlapping wavefunctions cause indistinguishability between forward and backward scattering, as depicted in Figure 2.5. The atomic wavefunctions are therefore symmetrized with respect to atom exchange, thus entangling the atomic spin states and leading to an effect that essentially rotates each atomic spin around their mean spin during collisions. Figure 2.6 shows an example of a single ISRE collision event in which two atoms with different spin rotate about their mean spin, leading to outgoing spins acquiring different spin orientations.

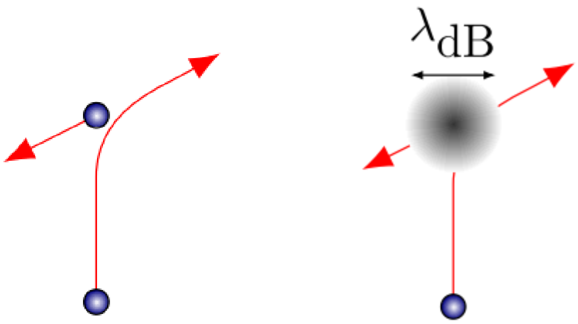

(a) (b)

Figure 2.5: Depiction of a collision of two atoms. In a) forward and backward scattering events are distinguishable. In b) the de Broglie wavelength is large and forward and backwards scattering events are indistinguishable. Figure from [25].

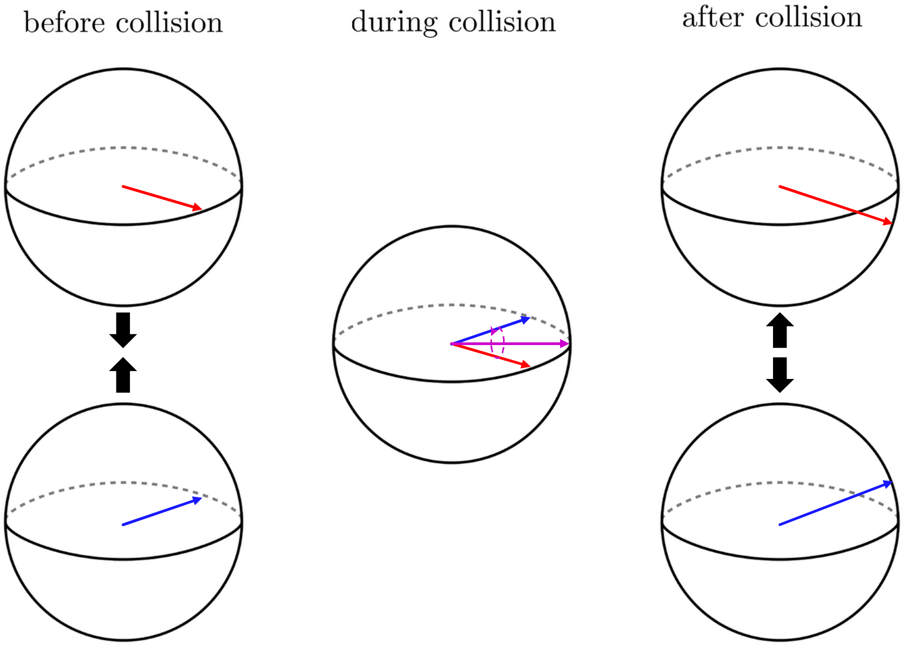

Figure 2.6: Example of an ISRE collision. Two spins with different fully transverse spin orientations collide. During the collision the spins rotate about their mean spin, shown in purple. The outgoing spins have acquired some longitudinal spin component.

Atomic clouds of Rb-87 used in this work are of temperature, $T = 650\text{nK}$, giving a de Broglie wavelength of $\lambda_{\text{dB}} = 230$ nm. The relevant collision length here is the s-wave scattering length $a \approx 5.2$ nm, which is much smaller than λ_{dB}. The s-wave scattering lengths of both spin states in Rb-87 are approximately the same. The strength of the ISRE, μ is given by the ratio of spin exchange scattering rate, ω_{exch}, to elastic scattering rate, τ^{-1}, that is, the ratio of coherent to randomizing collisions. The exchange scattering rate is determined by $\omega_{\text{exch}} = \frac{gn_0}{\hbar}$, where $g = 4\pi\hbar^2 a/m$ is the mean-field coupling constant, and n_0 is the peak atomic density of the atomic cloud. The radially averaged elastic collision time can be approximated by $\tau \approx (16a^2 n_0 \sqrt{\pi k_B T/m})^{-1}$. The details of this approximation are described in Reference [15]. $\mu < 1$ in the regime where the ISRE is not apparent. For the spin ensembles studied in this thesis $\mu = 8$, indicating that the ISRE has a strong effect on spin wave dynamics.

2.3.2 Quantum Boltzmann Equation

Spin diffusion of an atomic gas can be described by a quantum Boltzmann transport equation. References [14] and [15] give a full derivation. The atomic cloud used in our experiment is quasi-1D due to a high ratio of radial to axial trap frequency. We are therefore able to average over the radial dynamics as they occur significantly faster than the axial dynamics. In a quasi-1D atomic system atoms are able to move past one another in the axial direction by first translating radially, rather than in a truly 1D configuration, where atoms would need to exchange positions. Using a radially averaged spin distribution in phase-space, $\vec{m}(z,p,t)$, the 1D quantum Boltzmann equation is given as [15]

$$\frac{\partial\vec{m}(z,p,t)}{\partial t}+\frac{p}{m}\frac{\partial\vec{m}(z,p,t)}{\partial z}-\frac{\partial U_{\text{ext}}}{\partial z}\frac{\partial\vec{m}(z,p,t)}{\partial p}-\vec{\Omega}(z,t)\times\vec{m}(z,p,t)=\left.\frac{\partial\vec{m}(z,p,t)}{\partial t}\right|_{\text{1D}}. \tag{2.11}$$

Here U_{ext} is the harmonic trapping potential, which will be discussed in Section 3.4. The spin torque vector is given by $\vec{\Omega}(z,t)=\frac{1}{\hbar}[U_{\text{diff}}(z)\hat{z}+g\vec{M}(z,t)]$, where $U_{\text{diff}}(z)$ is the differential potential, which is the spatially varying energy difference between spin states, and $\vec{M}(z,t)$ is the spatial spin distribution. $\vec{M}(z,t)$ can be determined by integrating the radially averaged spin distribution over momentum space,

$$\vec{M}(z,t)=\frac{1}{2\pi\hbar}\int\vec{m}(z,p,t)\,dp. \tag{2.12}$$

The first term of Equation 2.11 represents the time evolution of the spin distribution, the second term describes the drift, and the third describes the force due to the external trapping potential. The final term on the left hand side is the spin-rotation term and includes the effects of both the ISRE as well as the Larmor precession due to spin-dependent potentials. This term describes the precession of spins around differential potentials and the local spin. From this term it is evident that the spin-wave dynamics in the system, resulting from spin-rotation effects, can be altered via a differential potential. This effect will be further discussed in Chapter 5. Lastly, the term on the right hand side of Equation 2.11 is the collision integral, which describes elastic scattering collisions. Simulations of the quantum Boltzmann equation are discussed in Chapter 5 and compared to experimental results.

Chapter 3

Experimental Procedure

The following Chapter outlines the experimental setup and methods used in this thesis to study spin diffusion of an ultracold Rb-87 gas. The experimental system discussed in Sections 3.2-3.5 and 3.7 is based off the work of H. J. Lewandowski, et al. [26], which was designed to be a robust apparatus to create and measure ultracold bosonic gases. Sections 3.6 and 3.8 describe how spin states are prepared and detected to study longitudinal diffusion of a two-domain spin profile. The procedure discussed in this Chapter is used in measuring the effects of domain wall width on longitudinal spin diffusion, with results presented in Chapter 5.

3.1 Overview

Rb-87 vapour is first loaded into a magneto-optical trap (MOT) located in a vacuum cell and cooled to the Doppler limit. The atoms are then transported to an ultra-high vacuum science cell. Within the science cell, atoms are trapped in a hybrid Ioffe-Pritchard magnetic trap and cooled to the desired temperature via evaporative cooling. Although this system can cool atoms past the critical temperature to create a BEC, the work done in this thesis uses atomic gases above degeneracy at $T = 1.6T_c$ and $T = 1.9T_c$. A two-domain spin state profile is prepared, using a beam of spatially varying laser intensity created with a digital micromirror device, and left to evolve in a differential potential. After some evolution time the atomic cloud is measured by absorption imaging. Cloud parameters are extracted from the resulting images to study spin state profiles and their evolution.

3.2 Magneto-Optical Trap

A Rubidium-87 vapour is loaded in the MOT vacuum cell using a Rubidium getter assembly. The getter assembly consists of a current running through a dispenser made of a stable Rubidium salt. The Rubidium vapour is cooled via Doppler cooling and then trapped within a spatially varying magnetic field. Doppler cooling is a technique that uses a laser detuned below an atomic transition to slow atoms. Any atom moving towards this beam will see the laser as being blue-shifted toward the atomic transition and is more likely to absorb a photon. The absorption of a photon decreases the atom's momentum. The atom will then re-emit the photon into a random direction. This process is repeated many times. Due to the isotropic nature of the emission events, the average momentum change due to photon emission is zero; therefore, the atom's net change of momentum is on average only due to photon absorption and thus in the opposite direction as its motion, leading to cooling. This effect can cool ensembles of atoms down to the Doppler temperature, $T_D = \frac{\hbar\Gamma}{2k_B}$, which is limited by spontaneous emission events leading to fluctuations in momentum.

The MOT traps and Doppler cools atoms using three sets of counter-propagating beams with opposite circular polarization and a set of magnetic coils in an anti-Helmholtz configuration. A diagram of the MOT set-up is shown in Figure 3.1. The coils produce a quadrupole magnetic field, which has a potential that has a zero between the two coils. Due to the Zeeman effect, levels are split into magnetic sublevels m_F. The circular polarizations of the beams are chosen such that, when in combination with the spatially varying Zeeman shift, they will drive atoms toward the center of the trap [27]. A simplified one-dimensional example of this is shown in Figure 3.2, where we see that if an atom is moving towards the right, away from the trap center, its transition frequency will become closer to the negatively shifted $m_F = -1$ state. The σ^- beam, propagating opposite to the atom's motion, can then drive the $\Delta m_F = -1$ transition, increasing the atom's photon scattering rate and pushing it back towards the center of the trap. Atoms moving to the left of the trap experience a similar effect with the σ^+ beam driving $\Delta m_F = +1$ transitions. In our MOT set-up, this process is more complicated, taking place in three orthogonal spatial directions. Further, for the cooling transition used, $5S_{1/2} \left|F=2\right\rangle \rightarrow 5P_{3/2} \left|F'=3\right\rangle$, the ground state and excited state have five and seven magnetic sublevels, respectively, rather than the one and three magnetic sublevels depicted in Figure 3.2.

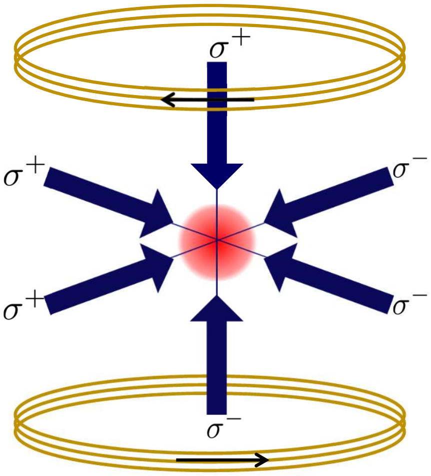

Figure 3.1: Diagram of the MOT. Atoms are trapped at the center using a combination of two current-carrying coils in an anti-Helmholtz configuration to produce a quadrupole magnetic field and three sets of counter-propagating laser beams. Black arrows indicate the direction of current through coils and blue arrows indicate the direction of laser propagation.

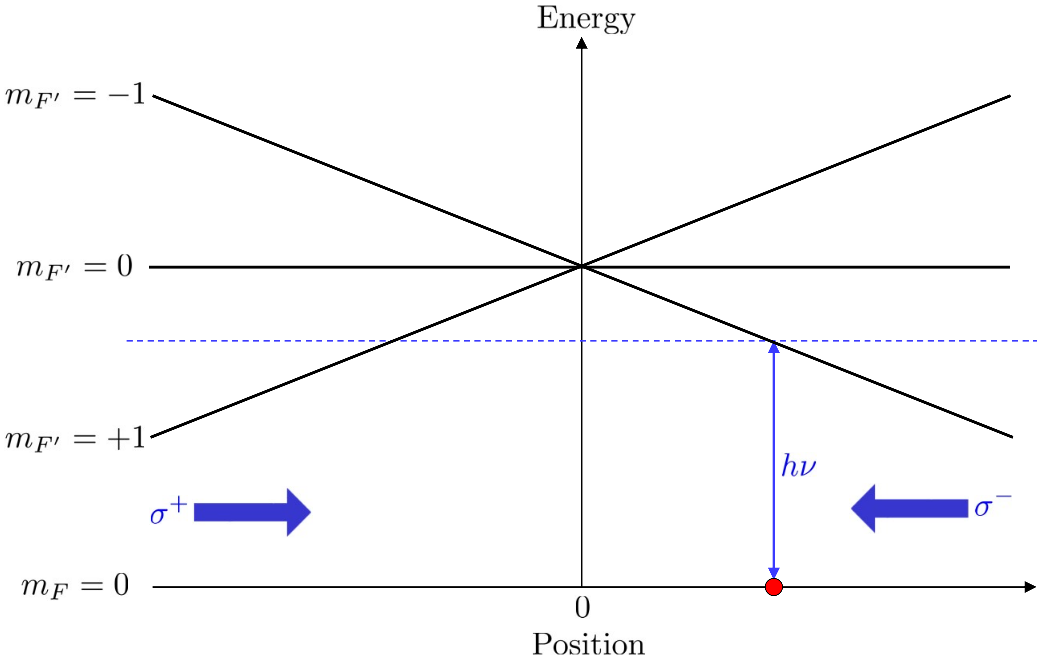

Figure 3.2: Example of a simplified 1D MOT. In the MOT the magnetic field Zeeman shifts the m_F sublevels. If an atom (shown in red) is located on the right, away from the trap center, the incoming σ^- beam will be resonant with the $\Delta m_F = -1$ transition, creating a scattering force towards the center of the trap.

The MOT uses a cooling laser that is red-detuned by about 20 MHz from the $5S_{1/2}\,|F = 2\rangle \rightarrow 5P_{3/2}\,|F' = 3\rangle$ transition. Off-resonant transitions can also excite atoms into the $5P_{3/2}\,|F' = 2\rangle$

state that may then decay to the $5S_{1/2}\,|F=1\rangle$ state. To put these atoms back into the cooling cycle, a repump laser locked to the $5S_{1/2}\,|F=1\rangle \rightarrow 5P_{3/2}\,|F'=2\rangle$ transition continuously excites these atoms until they decay into the $5S_{1/2}\,|F=2\rangle$ state. The cooling and repump laser transitions are shown in Figure 3.3.

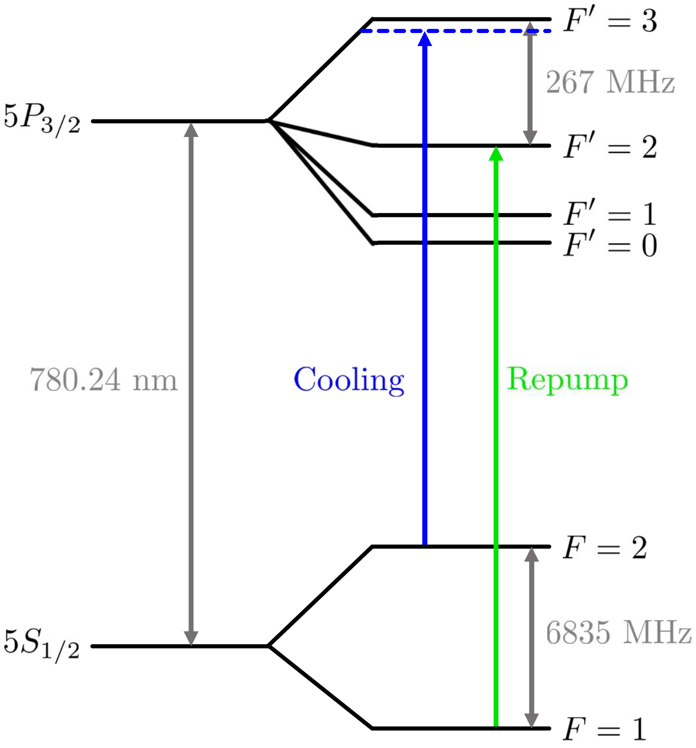

Figure 3.3: Energy level diagram of the hyperfine levels of $5S_{1/2}$ and $5P_{3/2}$ of Rb-87. The cooling laser is detuned from the $F=2 \rightarrow F'=3$ transition by ∼20 MHz. The repumping laser is resonant with the $F=1 \rightarrow F'=2$ transition.

3.3 Atom Transfer

After the MOT stage, atoms are transferred into a hybrid Ioffe-Pritchard (HIP) trap located within the ultra-high vacuum science cell to prolong atom lifetime by decreasing the number of collisions with background gases. For transfer, atoms are loaded into a tightly confined quadrupole trap. The tight confinement requires a strong magnetic field gradient. The strong magnetic field gradient increases the Zeeman shift, which causes atoms further from the center of the cloud to gain potential energy, causing heating during transfer. This effect is reduced by minimizing the spatial extent of the atomic cloud as much as possible by using a compressed MOT (CMOT) before transfer [28]. In the CMOT stage the intensity of the repump laser is reduced and the cooling laser is further detuned. By reducing the repump intensity the atoms spend less time in the $F=2$ state, and therefore less time resonant with the cooling laser. Detuning the cooling laser will reduce the photon scattering rate near the trap center, leading to a decrease in radiation pressure from scattered photons and a denser, smaller cloud of atoms.

Next, the repump beam is turned off to optically pump atoms into the $F = 1$ state. After pumping to the $F = 1$ state, atoms may be in any of the $m_F = 1, 0, -1$ hyperfine states. The magnetic field gradient is then adiabatically ramped up to trap atoms. Trappable states are those whose energy increases with increasing magnetic field. In low magnetic fields ($B < 0.1$ T), $m_F = -1$ is the only magnetically trappable state in $F = 1$, as seen in Figure 2.2, so atoms in $m_F = 0, 1$ exit the trap. Finally, the MOT coils are moved on a linear servo motor track toward the ultra-high vacuum science cell, where the atoms are transferred to a hybrid Ioffe-Pritchard trap.

3.4 Hybrid Ioffe-Pritchard Trap

The hybrid Ioffe-Pritchard trap consists of four electromagnetic coils and two permanent bar magnets oriented perpendicularly to the coils. The permanent magnets create a strong quadrupole field to radially confine atoms, while the coils provide axial confinement. The inner coils, referred to as the bias coils, produce a uniform magnetic bias field, B_0, while the outer coils, called the pinch coils, create axial curvature in the magnetic field. Near the center of the trap, the magnetic trapping potential can be approximated by [29]

$$U_{ext} \approx \frac{m}{2}(\omega_r^2 r^2 + \omega_z^2 z^2), \tag{3.1}$$

where m is the mass of atoms, and w_r and w_z are the radial and axial trap frequencies, respectively. The trap frequencies used in our experiment are $\omega_r = 2\pi \cdot 250$ Hz and $\omega_z = 2\pi \cdot 6.72$ Hz. As the strength of the axial-to-radial confinement is approximately 1:37, the atomic cloud is highly elongated in the axial directly, creating a quasi-one-dimensional geometry. Due to the high radial trap frequency, dynamics in the radial direction take place much faster than in the axial direction. We therefore average over the dynamics in the radial direction.

3.5 Evaporative Cooling

Once atoms are in the HIP trap, radio-frequency evaporative cooling is used to reduce the atomic cloud temperature past the Doppler cooling limit by removing the atoms with the most kinetic energy. Atoms with higher energy are generally located further from the trap center in areas of higher magnetic field, leading to a larger Zeeman shift between magnetic sublevels. By applying a radio-frequency field resonant with the $|1, -1\rangle$ to $|1, 0\rangle$ transition of atoms with the largest Zeeman shift, the highest energy atoms become untrapped. These atoms then leave the trap, carrying away excess energy. The remaining atoms rethermalize via elastic collisions to a lower temperature.

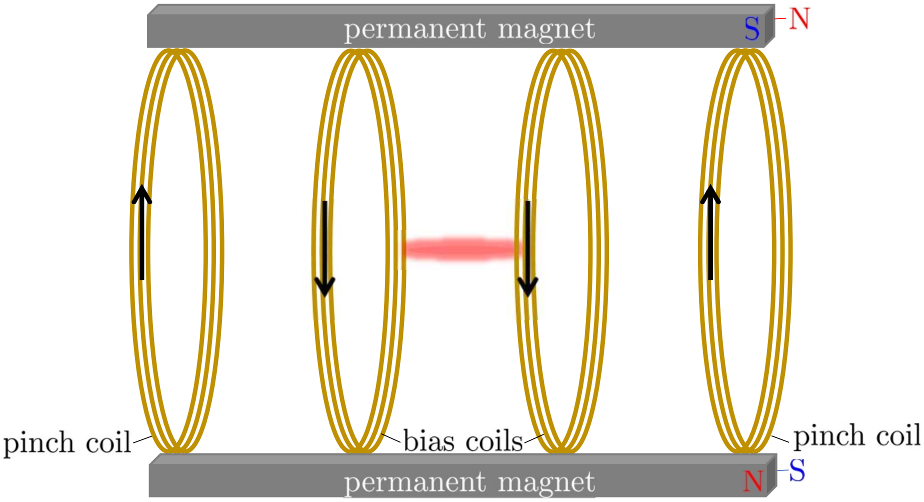

Figure 3.4: Diagram of the HIP trap setup. Two permanent magnets are used to confine atoms radially. Axial confinement is provided by coils. The bias coils create a uniform magnetic field and the pinch coils set the axial curvature of the field. Arrows indicate the direction of current through coils. North and south poles of the permanent magnet are labelled. The front facing side of the top magnet is south, and the back side (hidden) is north. The opposite is true for the lower magnet.

This process is repeated by exponentially sweeping the rf frequency from 60 MHz to ∼2 MHz to continuously remove the highest energy atoms, until the cloud is adequately cold. This process takes place over 10 stages. Each of the stages decreases the frequency to halfway to the trap bottom frequency. The final frequency of the i-th stage is given by

$$\nu_i = \frac{\nu_{i-1} - \nu_0}{2}. \tag{3.2}$$

ν_0 is the trap bottom frequency, which gives the energy difference between the $|1, -1\rangle$ and $|1, 0\rangle$ states in the center of the trap. In this experiment ν_0 is approximately 1.9 MHz. As the ensemble cools, the elastic collision rate changes and alters the time needed for rethermalization, so the time constant of each stage can be adjusted to optimize evaporation [27].

3.6 Spin Preparation and Evolution

Spin wave dynamics are highly dependent on the initial spatial distribution of spin states in the atomic cloud. This section describes the coupling of spin states, methods of preparing spin profiles using a digital micromirror device, and optimal preparation of a two-domain spin structure.

This thesis specifically explores two-domain configurations of pseudo-spin states $|1\rangle = |F = 1, m_F = -1\rangle$ and $|2\rangle = |F = 2, m_F = 1\rangle$, as described in Section 2.2.1. To conserve angular momentum, the states are coupled via a two-photon pulse. The two-photon pulse consists of a microwave pulse of ~6830 MHz, which is detuned from an intermediate state, $|F = 2, m_F = 0\rangle$, by approximately 700 kHz, and a radio-frequency pulse of ~3 MHz. This transition is shown in Figure 3.5.

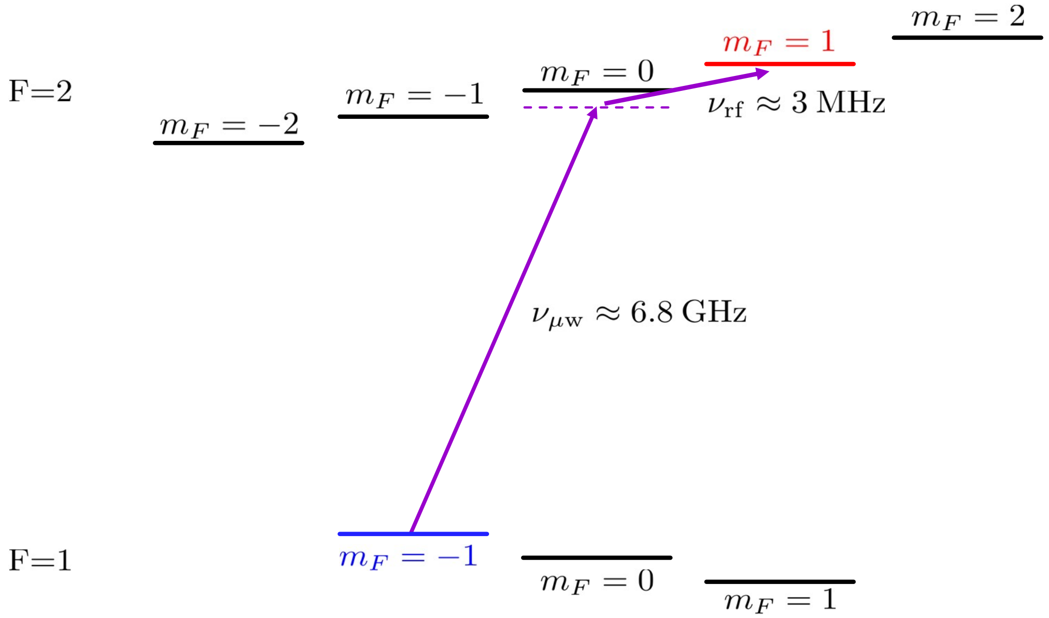

Figure 3.5: Energy level diagram of Rb-87 $5S_{1/2}$ manifold in magnetic field. The spin states comprising the pseudo-spin 1/2 system are $|1\rangle = |F = 1, m_F = -1\rangle$ and $|2\rangle = |F = 2, m_F = 1\rangle$, shown in blue and red respectively. Purple arrows depict the two-photon pulse connecting spin states, made up of a microwave and radio-frequency pulse.

Spin state profiles are created by applying a Stark-shift laser beam onto a digital micromirror device (DMD), which reflects an arbitrary pattern of the laser light onto the atomic cloud to Stark shift atomic energy levels where illuminated. A cloud-wide two-photon π-pulse will then transfer only the unilluminated atoms, those that are not Stark shifted, to the $|2\rangle$ state, leaving the Stark-shifted atoms in state $|1\rangle$. Atoms that are partially illuminated will be sent to a superposition state of $|1\rangle$ and $|2\rangle$.

The DMD is made of an 1024×768 array of independently controllable 13.6 μm mirrors. To create an arbitrary pattern, individual mirrors can be turned on/off, which tilts the mirror to $+/-12°$ [30], as shown in Figure 3.6a). When imaged onto the atoms with magnification of 1/12, the minimum feature size the DMD can create has a point spread function FWHM of 25 μm, corresponding to a 20 by 20 grid of mirrors on the DMD [25]. This resolution allows one to average over a group of 400 pixels to create an effective intensity between that of all mirrors on or off by turning on only a portion of the mirrors. The proportion of mirrors turned on or off in the group of 400 pixels, which determines the intensity of light reflected from the DMD image, is quantitatively described by the "pixel value". Pixel values range from 0, where all mirrors are off and no light is reflected from the DMD, to 255, where all mirrors are on and the full incoming laser intensity is reflected from the DMD. A pixel value between 0 and 255 results in an intermediate intensity of laser light reflected from the DMD. The method of averaging groups of mirrors to create intermediate reflected intensities essentially creates what appears as a greyscale image from a binary image.

Collimated light from the Stark-shift laser is directed toward the DMD, where only mirrors in the "on" state reflect light towards the atoms. An achromatic doublet lens located one focal length away from the atoms collects the reflected light and focuses the light pattern on the atoms. Figure 3.6b) shows the Stark-shift laser beam path from the DMD, where only half of the DMD mirrors are turned on, to the atomic cloud. The Stark-shift laser shifts energy levels via the AC Stark effect, dependent on the intensity of light reflected from the DMD. This effect is discussed further in Section 4.3. A two-photon π-pulse is applied to the entire atomic cloud, thus initializing the atomic cloud in an arbitrary spin-state geometry.

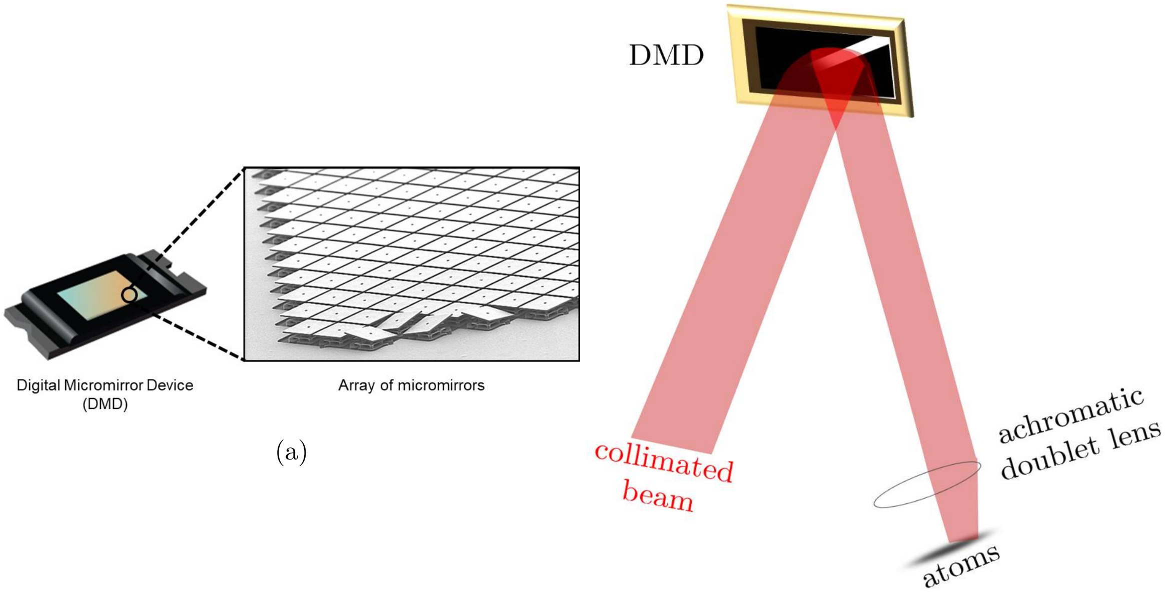

(a)

(b)

Figure 3.6: a) Image of DMD. Close ups show array of mirrors in various states (on/off/float) [31]. b) Schematic diagram of a laser beam reflected from a DMD and sent towards atomic cloud. The pattern on the DMD has only half of the mirrors in the on state, therefore only illuminating half of the cloud. Object sizes are not to scale.

The initial spin-state geometry used for all work done in this thesis is a two-domain configuration consisting of two longitudinal spin domains of spin $|1\rangle$ and $|2\rangle$, separated by a nearly fully polarized domain wall of width λ_0. Near full polarization of $\left|\vec{M}\right| \simeq 1$ is accomplished by a helical rotation of transverse spin between the longitudinal spin domains. Figure 3.7 depicts the transverse rotation of spin between longitudinal spin domains. To initialize the two-domain spin geometry the DMD is set up to contain an image varying from black to white with a hyperbolic tangent profile, as shown in Figure 3.8a). The resulting two-domain atomic cloud is shown in Figure 3.8b). To create the coherent helical transverse spin throughout the domain wall, half of the atomic cloud must be optimally detuned during a two-photon π-pulse. Reference [25] describes how using an optimal detuning minimizes phase wrapping of the transverse spin and maximizes the coherence in the domain wall. An optimal laser intensity sets the AC Stark shift to produce the optimal detuning of $\delta = \sqrt{3}\Omega_R$ for the two-photon microwave pulse. This preparation is used for all two-domain spin-state preparations in this thesis.

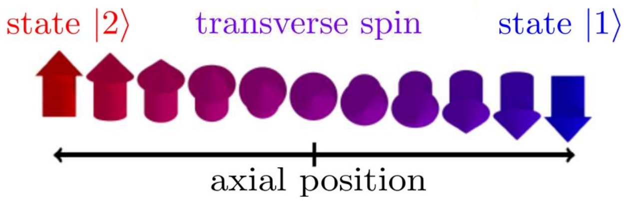

Figure 3.7: Initialization of spins within two-domain atomic cloud. State $|2\rangle$ atoms on the right have fully longitudinal spin. Through the domain wall atoms are rotated through the transverse plane forming a smoothly varying spin structure, ending in the longitudinal spin $|1\rangle$ state on the right [25].

After initializing the two-domain spin system, the atomic cloud is left to evolve for a given time period. During the evolution differential potentials may be applied to alter dynamics. These differential potentials are also created using the DMD and are discussed in Chapter 4. The atoms can then be measured using the imaging procedure described in Section 3.7, to study the longitudinal spin diffusion over time.

3.7 Imaging

Measurements of the atomic cloud are made using absorption imaging. This Section outlines the imaging procedure and processing.

3.7.1 Adiabatic Rapid Passage

Since there is no cycling transition from the $|1,-1\rangle$ state, atoms in the $|1,-1\rangle$ state must first be transferred to the $|2,-2\rangle$ state to be imaged. Adiabatic rapid passage (ARP) is used to coherently transfer atoms between states. ARP can be understood in the dressed state picture, where $|1,-1\rangle$ and $|2,-2\rangle$ are bare states, and when coupled by a radiation field the dressed states ($|+\rangle$ and $|-\rangle$) are linear combinations of the bare states. Figure 3.9 shows the dressed state picture as a function of microwave detuning.

If a far detuned coupling field is turned on, atoms initially in the $|1,-1\rangle$ state are placed in the $|-\rangle$ dressed state. The frequency detuning of the coupling field is adiabatically swept,

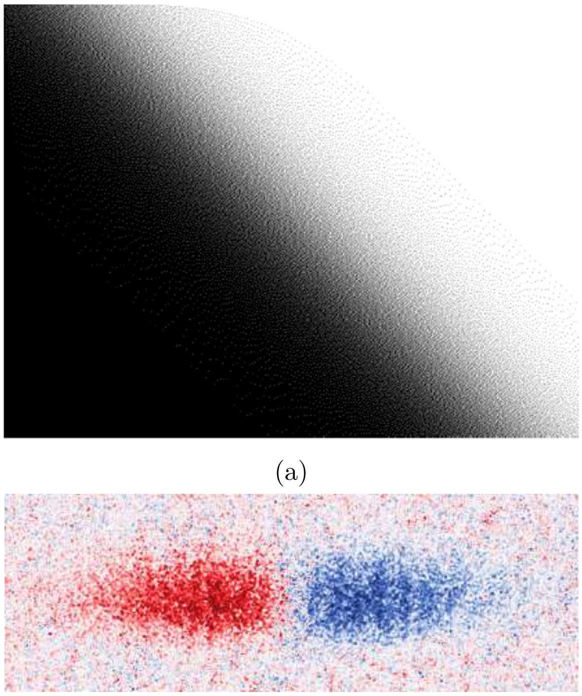

(a)

(b)

Figure 3.8: a) DMD pattern used to initialize two-domain spin-state profile. The image varies from black to white as a hyperbolic tangent. The DMD image is at an angle of 45° to the atoms as the DMD pixels rotate diagonally when in the on state. b) False colour image of atomic cloud in two-domain geometry. Red indicates spin $|2\rangle$ and blue indicates spin $|1\rangle$. [25]

such that atoms remain in the $|-\rangle$ dressed state. The probability of making a transition between dressed states is given by [32]

$$P = e^{-\frac{\pi}{2}\frac{\Omega_R^2}{\dot{\delta}}} \tag{3.3}$$

where $\dot{\delta}$ is the time rate of change of the microwave detuning. If the frequency detuning is swept slowly, compared to the square of the Rabi frequency ($\dot{\delta} \ll \Omega_R^2$), atoms will remain in the $|-\rangle$ dressed state. At some large, positive detuning, the coupling field is turned off and atoms will be transferred to the $|2,-2\rangle$ bare state with high efficiency.

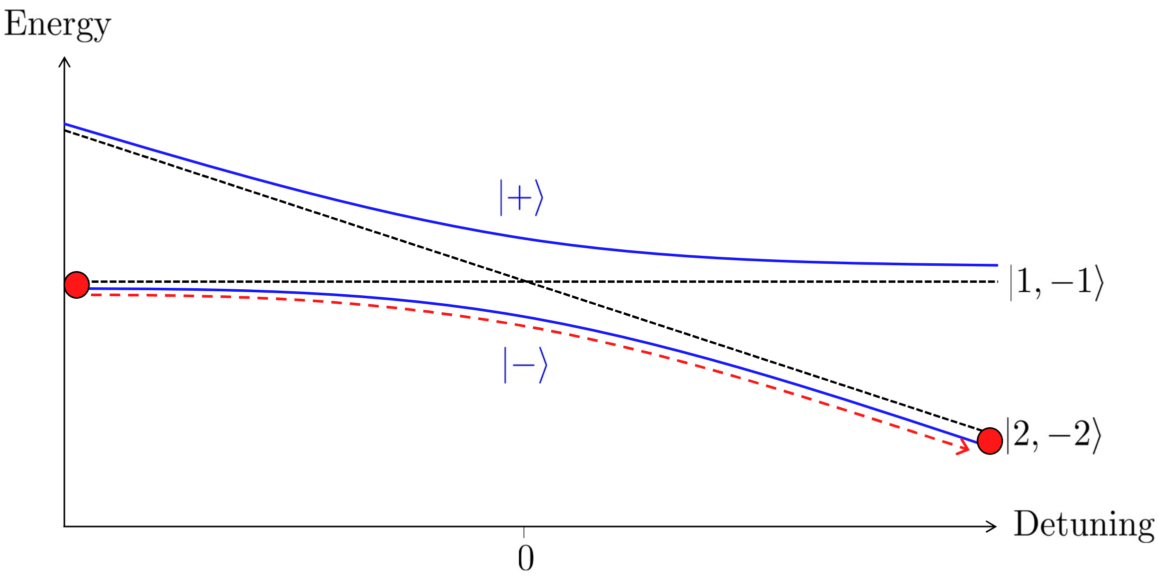

Figure 3.9: Illustration of energy levels as a function of detuning of bare states $|1,-1\rangle$ and $|2,-2\rangle$, and dressed states $|+\rangle$ and $|-\rangle$. If an atom, shown in red, is initially in the $|1,-1\rangle$ state, it can be transferred to $|2,-2\rangle$ via adiabatic rapid passage through the $|-\rangle$ state.

3.7.2 Imaging Procedure

In the $|2,-2\rangle$ state, atoms are anti-trapped, which causes the cloud to expand. To avoid saturation, the atomic cloud is expanded for 5 ms. To keep atoms in place a shim coil is used to apply a magnetic field to counteract gravity. Next the magnetic bias field is ramped to about 100 G to reduce the spatial variation of the magnetic field such that all atoms within the cloud will be resonant with a probe laser. To maximize photon scattering during imaging, the probe laser drives a cycling transition between $|2,-2\rangle$ and $|3,-3\rangle$ states. Images of the atomic cloud are taken using an CCD.

Atoms initially in the $|2\rangle$ spin state are unaffected by the ARP and do not scatter probe light, so they are not measured by absorption imaging. To measure the atom population in the $|2\rangle$ state, they must first be transferred to the $|1\rangle$ state by a π-pulse. They are then able to undergo ARP and the imaging procedure.

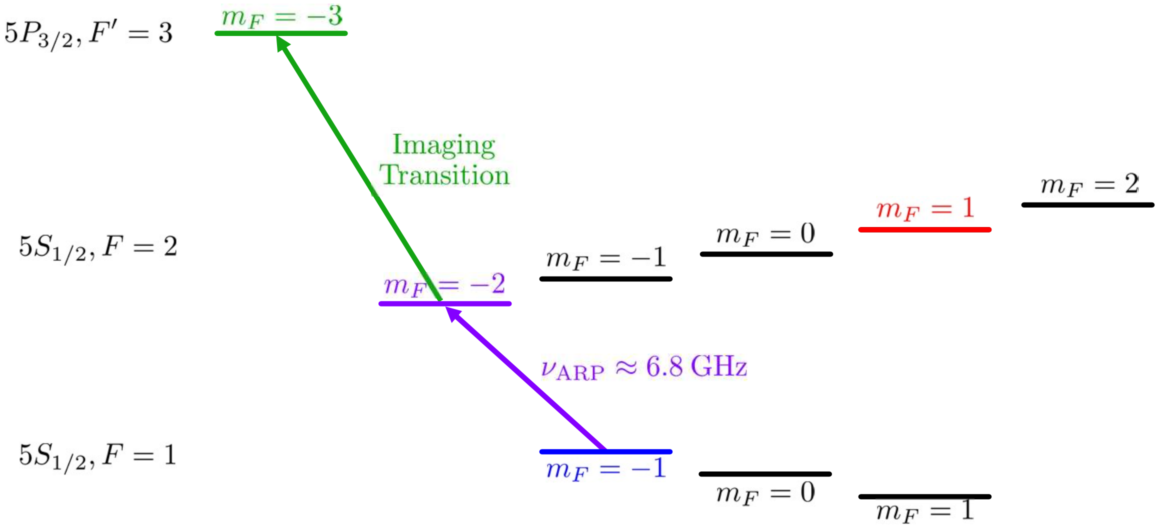

Figure 3.10: Energy diagram of the Rb-87 $5S_{1/2}$ and $5P_{3/2}$ levels. Imaging of the $|1,-1\rangle$ state is achieved by sending atoms to the $|2,-2\rangle$ state via ARP, and then a cycling transition is driven between the $|2,-2\rangle$ and $|3,-3\rangle$ states to maximally scatter photons.

3.7.3 Image Processing

As per Beer's law, the optical density (OD) of illuminated atoms can be determined as a function of I_0, the initial probe laser intensity, and I, the probe laser intensity after passing through the cloud of atoms. Beer's law is given by

$$OD = -\ln\left(\frac{I}{I_0}\right). \tag{3.4}$$

Along with the image of the atomic cloud, two additional images are taken for the purpose of normalization. The first is a "light" image, where the probe light is imaged without any atoms to give a measure of the maximum intensity, I_{light}. Second is a "dark" image, with the probe beam off and no atoms, with intensity I_{dark}, to measure dark currents and background scattered light. The OD can then be given by,

$$OD = \ln\left(\frac{I_{\mathrm{light}} - I_{\mathrm{dark}}}{I_{\mathrm{atoms}} - I_{\mathrm{dark}}}\right). \tag{3.5}$$

When using absorption imaging, there are two important systematic effects that must be accounted for. First is the effect of a minimum measured background intensity. Additional light may be captured by the CCD due to probe beam components that are off-resonant with the atomic cloud or probe light that does not pass through the cloud. These sources lead to some minimum intensity of probe light always reaching the CCD, resulting in a saturation optical density (OD_{sat}). To account for the saturation OD, the modified OD is calculated as

$$OD_{\mathrm{mod}} = \ln\left(\frac{1 - e^{-OD_{\mathrm{sat}}}}{e^{-OD_{\mathrm{meas}}} - e^{-OD_{\mathrm{sat}}}}\right). \tag{3.6}$$

Second, we must consider the effect of the probe laser intensity saturating the atomic transition. If the probe intensity is significantly less than the saturation intensity, I_{sat}, this effect can be accounted for by using

$$OD_{\mathrm{actual}} = OD_{\mathrm{mod}} + (1 - e^{-OD_{\mathrm{mod}}})\frac{I}{I_{\mathrm{sat}}}, \tag{3.7}$$

where $I_{\mathrm{sat}} = 1.67$ mW/cm^2 [26]. In our experiment the probe intensity is set to around $0.08 I_{\mathrm{sat}}$ to minimize the effect of this correction.

3.7.4 Image Fitting

After images are processed, data is axially binned and then they may be fit to extract the cloud's temperature, number of atoms, and density. Non-degenerate atomic clouds are fit with a 2D Gaussian, in the axial and radial directions, z and y. The 2D Gaussian is given by,

$$f_G = |OD_{\mathrm{peak}}| \exp\left(-\frac{1}{2}\frac{(z - z_c)^2}{(z_0')^2} - \frac{1}{2}\frac{(y - y_c)^2}{(y_0')^2}\right), \tag{3.8}$$

where z_c and y_c are the cloud centers, and z_0' and y_0' are the Gaussian widths of the atomic cloud after expansion time t.

From here the cloud's Gaussian width before expansion is determined by [26]

$$z_0 = \frac{z_0'\omega}{\sqrt{\omega^2 + (\omega^2 + \omega_0^2)\sinh^2(\omega t)}}, \tag{3.9}$$

where ω_0 and ω are the axial trap frequencies before and during expansion. A similar calculation is done for the radial direction y_0.

The temperature, number of atoms, and density of the atomic cloud can then be calculated by

$$T = \frac{m\omega_z^2 z_0^2}{k_B}, \tag{3.10}$$

$$N = 2\pi z_0 y_0 \frac{OD_{\mathrm{peak}}}{AC}, \tag{3.11}$$

and

$$n_0 = \frac{1}{(2\pi)^{\frac{3}{2}}}\frac{N\lambda_{\mathrm{trap}}^2}{z_0^3}, \tag{3.12}$$

respectively, where $\lambda_{\text{trap}} = \frac{\omega_r}{\omega_z}$ is the aspect ratio. The absorption cross-section is

$$AC = \frac{1}{2}\frac{3\lambda^2}{2\pi}\frac{1}{1+4\Delta^2/\Gamma^2}. \tag{3.13}$$

Here λ is the wavelength, Δ is the detuning, and Γ is the natural linewidth.

3.8 Longitudinal Spin Measurement

The longitudinal spin is reconstructed via two experimental runs. The first experimental run measures the population of state $|1\rangle$, N_1, while the second run measures the $|2\rangle$ population, N_2, by using an extra π-pulse to transfer atoms in $|2\rangle$ to $|1\rangle$ before imaging. Results from both experimental runs are combined to determine the cloud parameters and longitudinal spin profile at a given time.

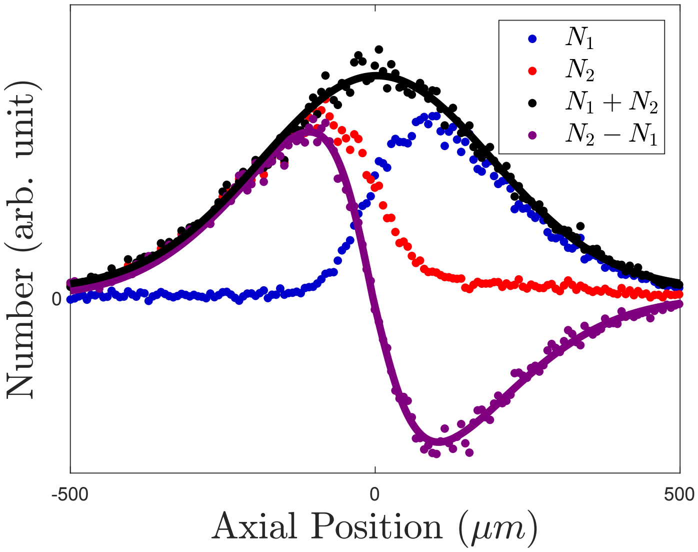

Figure 3.11: Atom populations of N_1 $|1\rangle$ (blue) and N_2 $|2\rangle$ (red) are measured via absorption imaging. The sum of the two populations (black) is fit with a Gaussian and represents the total density distribution. The difference of the two populations (purple) is the longitudinal spin and is fit with a hyperbolic tangent multiplied by a Gaussian and used to extract a domain wall width and position.

In general, the total spin is the quadrature sum of the longitudinal spin, M_z, and the transverse spin $M_\perp$. Transverse spin can be measured using Ramsey spectroscopy. Details of this type of measurement can be found in Reference [25]. Transverse spin measurements are not included in this thesis and fully coherent transverse spin is assumed in calculations. For fully coherent spins the total spin of the atomic cloud is given by $N_1 + N_2$, which when fit with a Gaussian allows for the determination of temperature and density as discussed in Section 3.7.4.

The longitudinal spin is defined as

$$M_z(z) = \frac{N_2(z) - N_1(z)}{N_2(0) + N_1(0)}. \tag{3.14}$$

Here longitudinal spin is divided by the peak number so that $-1 \leq M_z \leq 1$. Figure 3.11 shows an example of the measurements of total and longitudinal spin from populations N_1 and N_2. For a two-domain system the longitudinal spin is fit by the phenomenological model

$$M_z(z) = A \tanh\left(\frac{z - z_c}{\lambda}\right) \exp\left(\frac{-(z - z_c)^2}{2z_0^2}\right), \tag{3.15}$$

where A is the amplitude, λ is the domain wall width, z_c is the center position of the domain wall, and z_0 is the Gaussian width determined from the $(N_1 + N_2)$ Gaussian fit. Figure 3.11 shows measurements of the $|1\rangle$ and $|2\rangle$ atom populations, as well as their sum and difference. The sum, shown in black, is fit with a Gaussian, and the difference, shown in purple, is fit with the model in Equation 3.15.

The experimental sequence is repeated, and the longitudinal spin is calculated for a variety of spin evolution times to investigate the longitudinal spin dynamics. Results are plotted in a false colour spatio-temporal plot. At long time scales, much of the $|2\rangle$ population may be lost due to dipolar relaxation. To account for the loss of spin, a normalized longitudinal spin can be used,

$$M_z^N(z) = \frac{N_2(z)}{N_{2,\mathrm{tot}}} - \frac{N_1(z)}{N_{1,\mathrm{tot}}} \tag{3.16}$$

where $N_{\mathrm{i,tot}}$ is the sum of spin populations across all axial bins at a given time. This normalization assumes there is a 50:50 distribution of N_1 and N_2. Figure 3.12 shows a comparison of normalized and unnormalized spin evolution profiles. The use of normalized spin does not have a significant effect on the parameters of interest describing the spin dynamics, for instance damping and oscillation frequencies.

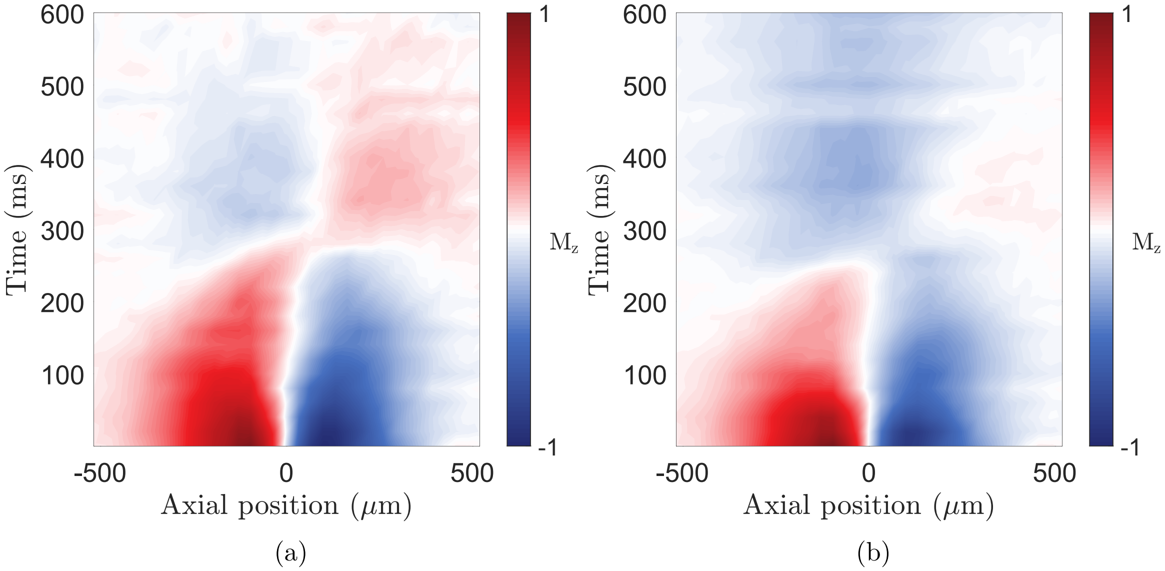

(a)

(b)

Figure 3.12: (a) Normalized and (b) unnormalized false colour spatio-temporal plot of a two-domain spin evolution. The normalized plot gives a better visual representation of spin dynamics at long times as it accounts for loss of $|2\rangle$ atoms.

Chapter 4

Differential Potential Measurement and Control

Atoms in states $|1\rangle$ and $|2\rangle$ experience a differential potential based on variations in the energy splitting between them. The differential potential acts as an effective magnetic field, modifying spin dynamics in our experimental system; Thus it is necessary to have the tools to accurately measure and control potentials. This Section first outlines the method of Ramsey interferometry that is used to measure frequency differences between the two spin states. Next, the cancellation spot is discussed, which results in a uniform differential potential across the atomic cloud. Lastly, the AC Stark effect is reviewed and a procedure for correcting inhomogeneities in externally applied differential potentials is outlined.

4.1 Ramsey Interferometry

Ramsey interferometry is a well known method used to determine the transition frequency between two states [33]. The Ramsey method used in our experiment starts with a $\pi/2$-pulse, resonant with the two-photon transition, to initialize spins in an equal superposition of $|1\rangle$ and $|2\rangle$. The spin then evolves for some evolution time, T, allowing the phase of the superposition state to evolve in proportion to the energy difference between the states. The detuning, δ, is the frequency splitting between the two states relative to the fixed frequency oscillators. Lastly, another $\pi/2$-pulse recombines the states for read-out. The initialization and read-out pulses can be of other lengths, but are chosen to be $\pi/2$-pulses to maximize the signal-to-noise ratio. Figure 4.1 shows this pulse sequence.

The probability of finding an atom in the excited state after this Ramsey sequence is [26]

$$P(T) = \frac{1}{2} + \frac{1}{2}\cos(\delta T) \tag{4.1}$$

under the conditions of small detuning ($\delta \ll \Omega_R$) and short pulse lengths ($t_{\pi/2} \ll T$). The $|1\rangle$ population is measured at a given T. This process is repeated for various evolution times, and oscillations of atom population between the states can be mapped out as a function of evolution time, resulting in Ramsey fringes of frequency δ. Ramsey frequencies are fit separately for each axial bin across the entire atomic cloud to determine the spatial frequency profile of the differential potential. An example of this process is shown in Figure 4.2. Figure 4.2b), shows the resulting differential potential across the atomic cloud, with error bars indicating the uncertainty in the sinusoidal frequency fits for each axial position. At the edges of the atomic cloud, where density of atoms is much lower, there is a low signal-to-noise ratio in measurements, resulting in reduced quality of fits and large error bars.

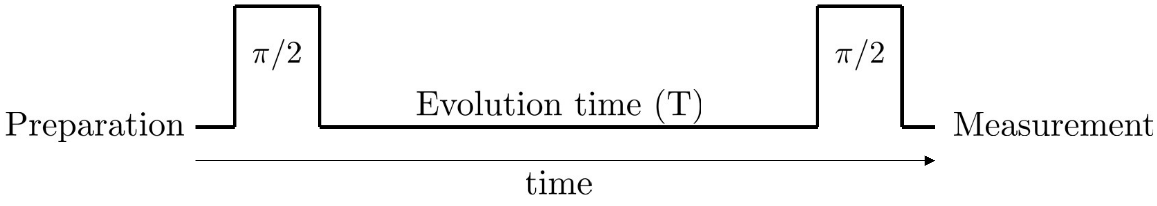

Figure 4.1: Diagram of the Ramsey pulse sequence.

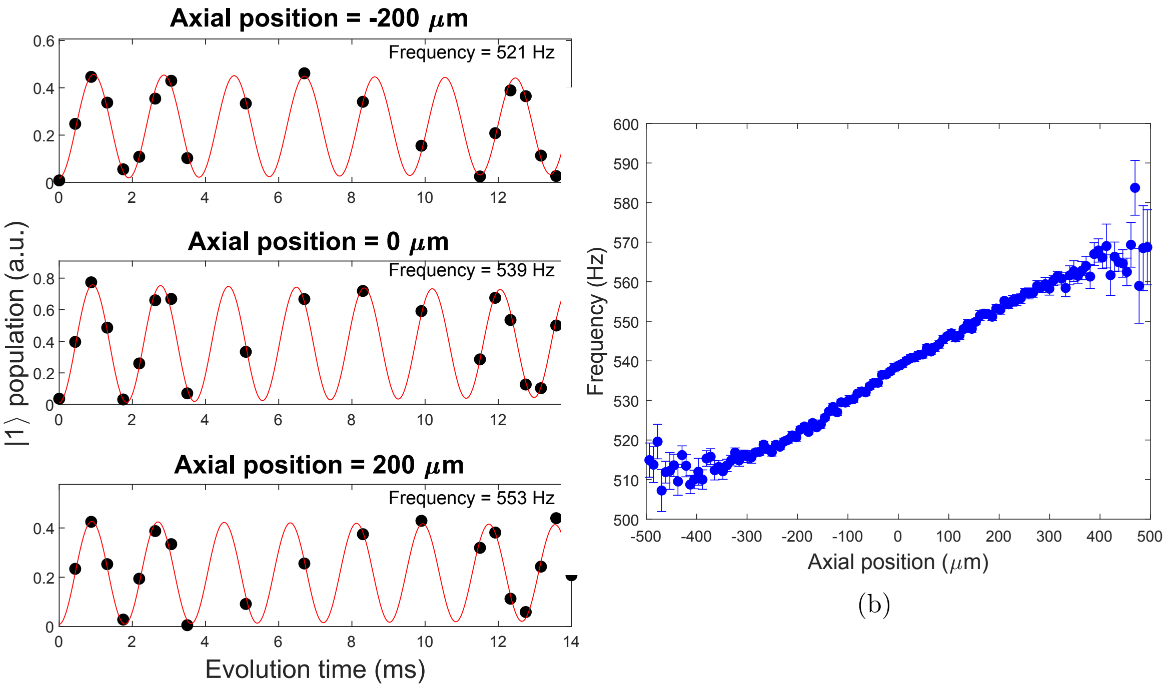

(a)

(b)

Figure 4.2: Example of using Ramsey interferometry to measure a differential potential. In a) each black dots represents the state $|1\rangle$ population at a point in time. Each plot shows the frequency measured at a different axial position of the atomic cloud. Frequencies are measured for all axial bins and then plotted in b) to measure the overall spatial frequency profile. The frequency measured is the difference between the detuned oscillator and the transition frequency between states.

4.2 Cancellation Spot

The total differential potential between spin states is a result of the Zeeman shift, mean-field shift, and any additional applied potentials. The additional potentials will be discussed further in Section 4.3. In the absence of an additional applied potential, a cancellation spot can be found, which results in a uniform differential potential.

In an intermediate magnetic field, the Breit-Rabi formula describes the Zeeman shift (Equation 2.4) and predicts a minimum transition frequency between the two states at a bias field of $B = 3.23$ G, which is referred to as the "magic spot." We work slightly below the magic spot, at the cancellation spot ($B_0 \approx 2.9$), where the mean field shift and Zeeman shift approximately cancel, such that no differential potential is experienced between the spin states unless applied using laser-generated potentials. In our experiment, the Zeeman shift has a parabolic spatial profile due to the dependence of the Breit-Rabi formula on the magnetic trapping field, which is parabolic in the axial direction in the regions we operate.

The mean-field shift arises from atom-atom interactions and is given by [34]

$$\Delta E_{MF}(z) = \frac{4\pi\hbar^2}{m}\Big[2a_{22}n_2(z) - 2a_{11}n_1(z) + 2a_{12}\big(n_1(z) - n_2(z)\big)\Big] \tag{4.2}$$

where m is the atomic mass, a_{ij} is the s-wave scattering length between states i and j, and n_i is the density of atoms in state i. The mean-field shift scales with density and thus has a Gaussian spatial profile.

For a given density, the bias field of the HIP trap can be adjusted such that the Zeeman shift and mean-field shift approximately cancel. A schematic of the cancellation spot is shown in Figure 4.3. As the Zeeman shift has a parabolic spatial profile in the HIP trapping potential and the mean-field shift has a Gaussian profile, the total differential potential is never completely flat, but care is taken to ensure that it is as flat as possible at the center of the cloud. The differential potential is measured using Ramsey spectroscopy to confirm we are working at the cancellation spot. A measurement of the cancellation spot can be seen in Figure 4.4.

4.3 AC Stark Effect

Spin-state preparation and the application of external differential potentials both make use of the AC Stark effect. The Stark-shift laser produces an oscillating electric field that shifts energy levels via the AC Stark effect. The interaction potential between the electric field, $\vec{E}$, and the induced atomic dipole moment, $\vec{p}$, is

$$U_{\text{dip}}(z) = -\frac{1}{2}\langle \vec{p} \cdot \vec{E} \rangle. \tag{4.3}$$

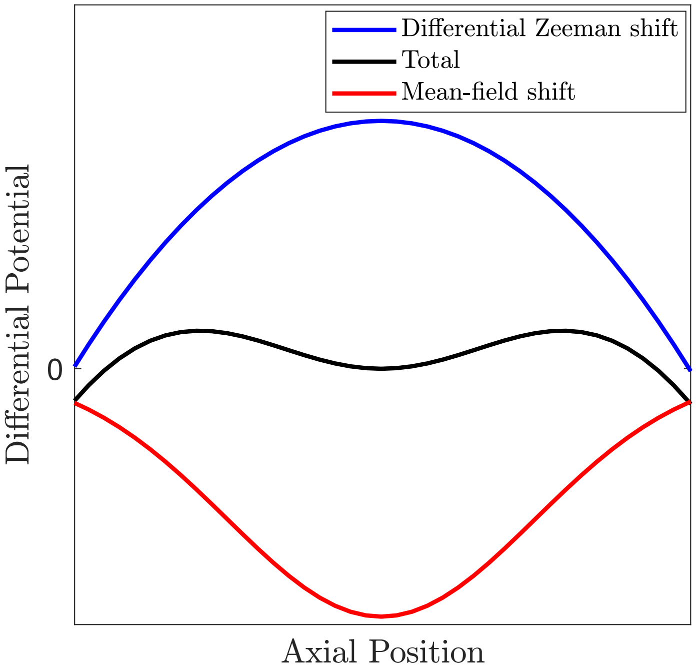

Figure 4.3: Schematic representation of the cancellation of the differential potential of the parabolic Zeeman shift, shown in blue, and the Gaussian mean-field shift, shown in red.

For laser detuning, ω, near the D_2 transition, the dipolar potential is given by [35],

$$U_{\text{dip}}(z) = \frac{\pi c^2 \Gamma}{2\omega_0^3}\left(\frac{2+\mathcal{P}g_F m_F}{\omega-\omega_0}\right)I(z). \tag{4.4}$$

Here ω_0 is the transition frequency between $5S_{1/2}\left|F\right\rangle$ and $5P_{3/2}$ level, Γ is the spontaneous decay rate from the excited state, and $I(z)$ is the spatial intensity distribution of the laser. $\mathcal{P}$ is the polarization of the laser, which is zero for linear polarized light and ± 1 for circularly polarized light.

Spin states $\left|1\right\rangle$ and $\left|2\right\rangle$ experience different dipolar potentials. The differential potential is then defined as $U_{\text{diff}} = U^{(2)}_{\text{dip}} - U^{(1)}_{\text{dip}}$. The spatial profile of the laser intensity after reflection from the DMD shifts atomic energy levels to create arbitrary differential potential profiles across the cloud. The effects of various differential potentials on spin evolution is discussed in Chapter 5. Figure 4.4 shows the spatial profile of a flat differential potential, found at the cancellation spot, compared to a positive linear gradient differential potential created using the Stark-shift laser.

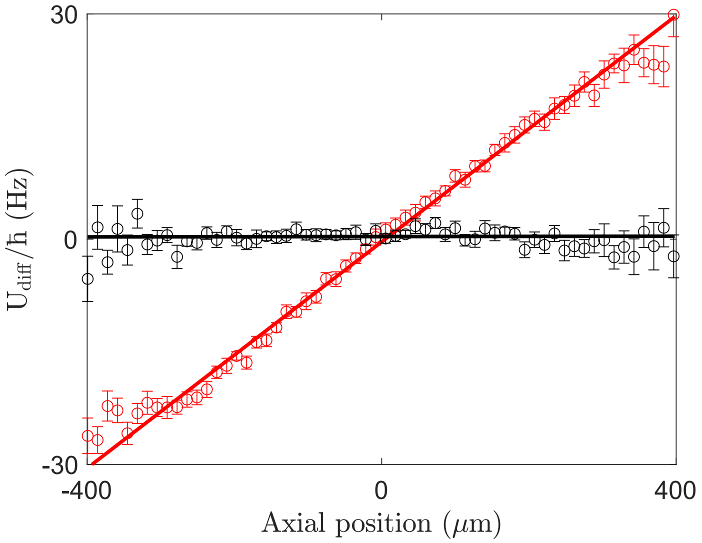

Figure 4.4: A flat differential potential at the cancellation spot (black) compared to a positive linear differential potential gradient of $G = 75$ Hz/mm (red). Differential potentials were measured using Ramsey spectroscopy (Section 4.1).

4.4 Stark-Shift Laser Correction

As discussed in Section 4.3, the Stark-shift laser shifts atomic energy levels due to the AC Stark effect. The Stark-shift laser is used to initialize spin states and create arbitrary differential potentials. In our experimental set-up, when the Stark-shift laser was applied to the atomic cloud, via the path shown in Figure 3.6b), it produced an unexpected non-uniformity in the spatial transition frequency profile. Figure 4.5a) shows an example of the frequency profile of the Stark shift laser reflected fully from the DMD, measured via Ramsey spectroscopy. For a laser beam with no distortion along the optical path, we expect a flat frequency across the atomic cloud. Our measurements show a clear non-uniform frequency across the atomic cloud. A non-uniform intensity hinders us from creating the desired linear differential potentials and initializing optimal spin-state profiles in a simple way. Fortunately, the versatility of the DMD offers a convenient solution to this problem. A corrected pattern is created to counter-act the non-uniformity, such that areas of higher beam intensity can be lowered by decreasing the light reflected from the DMD, by changing the pixel value of groups of mirrors.

A corrected pattern is created by first measuring the Ramsey frequencies resulting from full intensity reflection from the DMD, with all pixel values set to 255. The intensity of the Stark-shift laser is chosen such that the measured Ramsey frequencies for all axial positions lie above the optimal detuning, $\delta = \sqrt{3}\Omega_R$. The high laser intensity allows for the reduction of frequency to reach the optimal detuning. We choose the optimal detuning as a target frequency so that when the Stark-shift laser is used for spin-state preparation it results in maximum coherence in the domain wall, as discussed in Section 3.6.

Next, Ramsey frequencies are measured for two slightly lower effective pixel value settings, resulting in one Ramsey frequency profile close to optimal detuning and one below optimal detuning. Figure 4.5b) shows the resulting frequencies from the three Ramsey measurements compared to the optimal detuning frequency. For each axial position the frequencies are linearly interpolated to find the pixel values corresponding to the optimal frequency. A DMD pattern can be constructed with the resulting effective pixel values to create a uniform frequency profile at $\delta = \sqrt{3}\Omega_R$. Figure 4.5c) shows the frequency profile measured by setting the DMD to the corrected pattern.

Occasionally the corrected frequency profile still shows some non-uniformities, as the interpolated pixel values corresponding to frequencies may be slightly incorrect due to noise and uncertainty in measurements. In this case the profile can be iteratively improved by changing the pixel values of the DMD pattern for calibration measurements in smaller step sizes, and thus adding more points to the interpolation, leading to more accurate results. Once a corrected pattern is made, the resulting pattern can be multiplied onto a hyperbolic tangent DMD pattern used for spin initialization [Figure 3.8a)] or a linear gradient pattern to create the desired differential potentials.

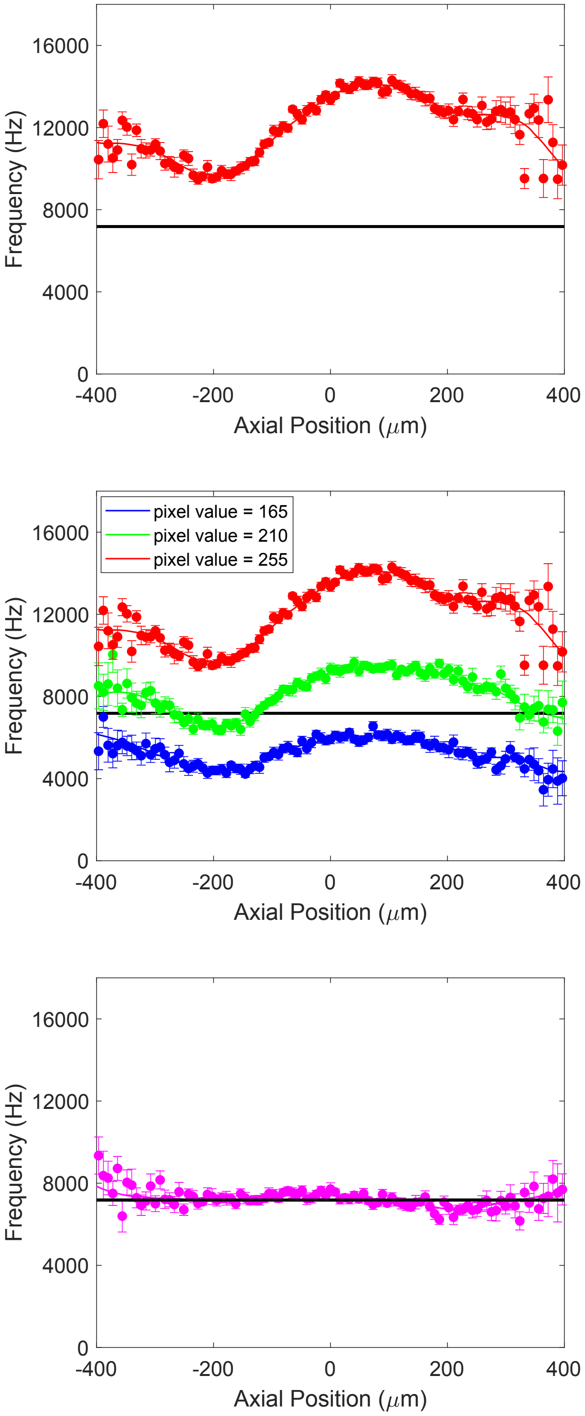

(c)

Figure 4.5: Ramsey frequency measurement of Stark-shift laser on atoms after a) full intensity reflection from DMD, b) reflection from DMD at various pixel values, c) reflection from DMD using corrected pattern. The black line in all plots shows the optimal detuning frequency for profile creation of $\delta = \sqrt{3}\Omega_R$.

Chapter 5

Longitudinal Spin Diffusion Dynamics

This Chapter investigates the effects of domain wall width on the longitudinal spin diffusion of a two-domain ultracold gas of Rb-87 above degeneracy. First, Section 5.1 discusses previous studies on spin diffusion in a non-degenerate bosonic gas. In Section 5.2 we analyze the spin diffusion dynamics at various domain wall widths, both in a flat differential potential and a positive linear differential potential gradient. In Section 5.3, a method of determining a stabilizing linear potential gradient corresponding to an equilibrium domain wall width is discussed. Results are compared to theoretical predictions in the hydrodynamic limit.

5.1 Background

The McGuirk group has been working towards determining the effects that altering various experimental parameters have on spin-wave dynamics, and understanding the role quantum interactions, such as the ISRE, play in these dynamics. Previous studies have explored methods of controlling spin diffusion in a two-domain non-degenerate gas by altering the amount of coherence in the domain-wall, and by applying differential potential gradients to the atomic cloud.

In the paper "Longitudinal spin diffusion in a nondegenerate trapped Rb-87 gas" [16], the authors examined the role that coherence of a helical transverse spin domain wall has on longitudinal spin diffusion. They showed that when the domain wall is initialized with a highly coherent transverse spin, longitudinal spin diffusion lifetimes are extended up to ten times compared to classical diffusion lifetimes. Within a coherent domain wall the helical transverse spin allows for ISRE collisions to rotate an atoms spin to follow the local transverse spin as it moves across the cloud, hence for many collisions through the domain wall an atom's spin is adiabatically rotated from $|1\rangle$ to $|2\rangle$ or vice versa. Low coherence will effectively randomize the transverse spin phases; hence ISRE collisions do not allow for spins to be adiabatically rotated across the cloud. Longitudinal spin-waves for the case of lower coherence shows shorter lifetimes and increased oscillation frequencies, reaching the classical diffusion case when coherence is zero.

Another study using highly coherent domain walls demonstrated that spin diffusion dynamics are further altered by the application of differential potential gradients as they change the relative precession rates and therefore orientation of transverse spins between the longitudinal spin domains. The addition of a linear differential potential gradient has been shown to speed or slow spin wave oscillations, depending on the sign of the gradient with respect to the diffusive spin current [17]. This is a result of two mechanisms generating spin currents. The first is a diffusive spin current generated by the transverse helical spin domain wall, which drives the system towards equilibrium. The second is an ISRE-generated spin current due to the Larmor precession of spins, which is further modified by differential potential gradients. In a positive linear potential gradient, as shown in Figure 4.4, the ISRE-generated spin current counteracts the diffusive spin current, resulting in a decreased net spin current, leading to long-lived stable spin domains. Conversely, a negative linear potential gradient will increase oscillation frequencies and speed up diffusion, as the ISRE-generated spin current adds to the diffusive spin current. The effects of these various differential potentials on longitudinal spin diffusion can be seen in Figure 5.1.

The transverse spin was also shown to exhibit a transverse spin-wave that is decoupled from the longitudinal spin and is confined to be within the domain wall. This spin-wave behaviour shows a stark contrast to that of a transverse spin wave in a uniform differential potential, where coupling of the transverse and longitudinal spin-waves is observed. This paper then describes a method of determining the magnitude of differential potential gradients required to stabilize a domain wall for atomic clouds of various temperatures and densities by analyzing the domain wall relaxation rate.

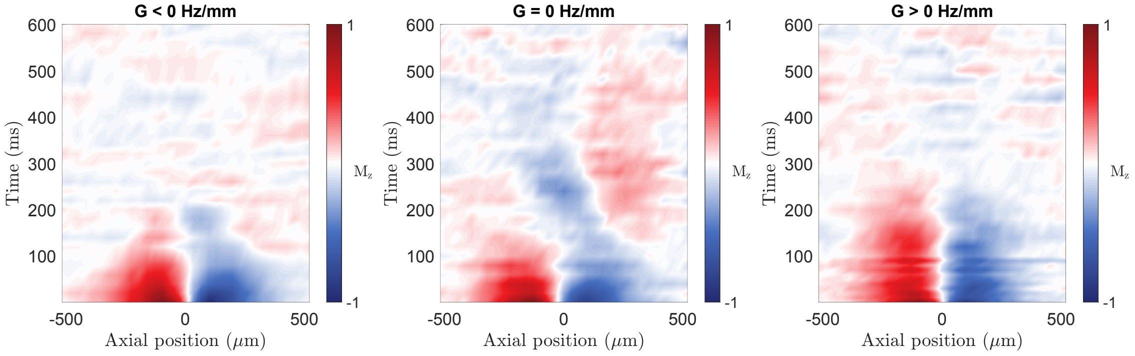

(a) (b) (c)

Figure 5.1: False colour plots of two-domain longitudinal spin diffusion dynamics in a) a negative linear differential potential gradient, b) uniform differential potential at the cancellation spot, c) a positive linear differential potential gradient.

These studies have given us a better understanding of how the ISRE modifies spin dynamics, and expanded our knowledge on how to control spin-waves. The following work builds off of these previous studies to understand another parameter effecting spin-diffusion: the domain wall width. The following sections use highly coherent domain walls to determine the effects of domain wall width on longitudinal spin diffusion, both in a uniform differential potential and in a positive linear gradient differential potential. Section 5.3 uses a method similar to that of Reference [25] to explore the relationship between equilibrium domain wall widths and stabilizing differential potential gradients.

5.2 Effects of Domain Wall Width on Longitudinal Spin Dynamics

As domain wall width determines the number of ISRE interactions an atom experiences while moving through a domain wall, it is expected to play a large role in the resulting spin-wave dynamics observed in an atomic cloud. However, as ISRE collisions are complicated events, it is sometimes difficult to exactly anticipate how the spin-wave dynamics will be affected. To understand the effects of domain wall width, longitudinal spin evolution data is collected for various domain wall widths.

Experimental data discussed in this Chapter was collected following the procedures outlined in Chapter 3. Atoms are first cooled within a MOT, and then evaporatively cooled further in a HIP trap. A fully polarized two-domain longitudinal spin system is prepared with an initial domain wall width, λ_0. The domain wall has a coherent helical transverse spin throughout, as shown in Figure 3.7. The structure is initialized in an atomic cloud with $n = 1.4 \times 10^{13}$ cm^{-3} and $T = 650$ nK $= 1.9T_c$, and allowed to evolve for up to 600 ms, either in the uniform differential potential at the cancellation spot (Section 4.2) or in a linear potential gradient. To quantify the dynamics of the two-domain system, the dipole moment at each point in time is calculated as

$$\langle zM_z \rangle = \frac{1}{n} \sum_{i=1}^{n} z_i M_z(z_i, t) \tag{5.1}$$

where n is the number of axial bins. For a two-domain spin system where symmetry about the trap center is preserved, the dipole moment should give an accurate representation of the longitudinal spin dynamics.

For comparison, numerical simulations of the quantum Boltzmann equation (Equation 2.11) were performed using a Crank-Nicolson alternating-direction finite difference technique, similar to the process outlined in [15, 25]. Toy models of the initial transverse and longitudinal spin distributions, as well as experimental parameters such as the cloud temperature, density, and trap frequencies are used to initialize the simulations.

5.2.1 Spin Dynamics in a Uniform Differential Potential

We first aim to study the effects of domain wall width in a two-domain system in the absence of an external applied differential potential. After spin-state preparation the spins evolve in a uniform differential potential at the cancellation spot. False colour plots of the spin diffusion dynamics for two different domain wall widths are shown in Figure 5.2. In all cases spins exhibit collective behaviour resulting in damped spin wave oscillations. For domain wall width $\lambda_0 = 69\ \mu$m, the spin profile oscillates and shows a complete flip of spin distribution after approximately 300 ms, such that the left side of the cloud is in $|1\rangle$ and the right is in $|2\rangle$, opposite to the spin distribution at $t = 0$. For $\lambda_0 = 132\ \mu$m, the spin distribution shows slower oscillation as it does not completely flip within the measured 600 ms. Classically we would expect the spin distribution to flip at half a trap period, which is approximately 75 ms in our experiment.

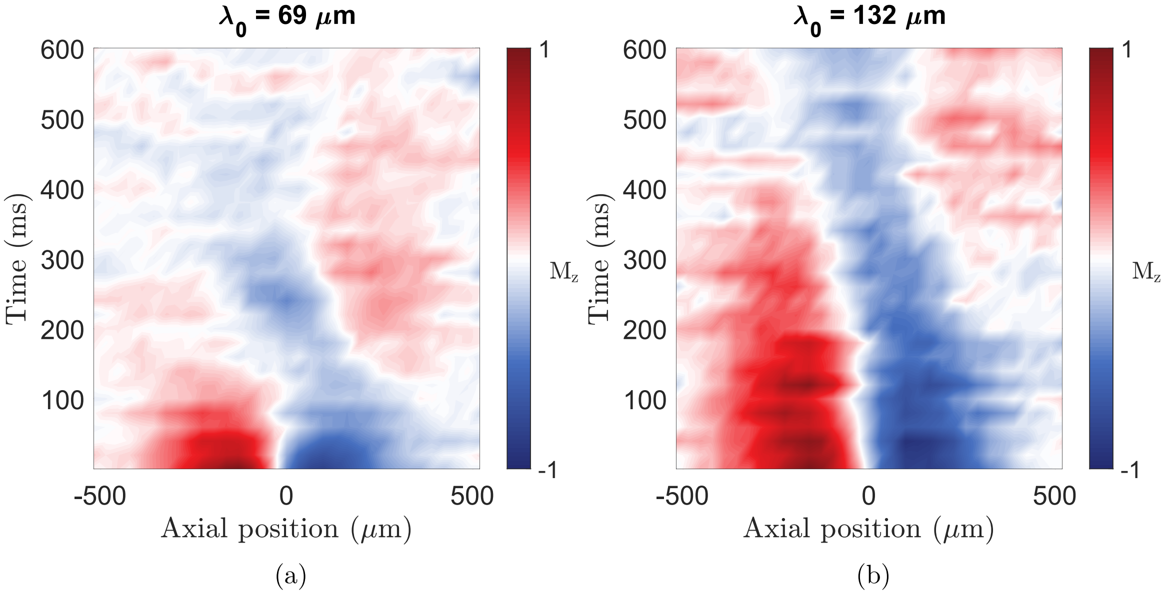

Figure 5.2: False colour plots of spin diffusion dynamics in a uniform differential potential for a two-domain preparation with domain wall width a) $\lambda_0 = 69\ \mu$m and b) $\lambda_0 = 132\ \mu$m. The domains prepared with a $\lambda_0 = 132\ \mu$m exhibit much slower oscillations and an extended lifetime in comparison to the domains prepared with $\lambda_0 = 69\ \mu$m. Note that false colour plots do not give an accurate visualization of domain wall widths. Instead, longitudinal fits at a given time (as in Figure 3.11) can be used to visualize domain wall widths.

For each dataset with different initial domain wall widths, the dipole moment is calculated via Equation 5.1 for each measurement in time. The results are fit to a damped sinusoid of the form $A\exp(-\Gamma t)\sin(2\pi f t + \phi)$. Examples of the damped sinusoidal fits to the time evolution of the dipole moment are shown in Figure 5.3. Questions remain as to whether the dipole moment phase, ϕ, should be a fixed parameter. One might expect the phase of all dipole moments to be the same, as spin currents are initialized in the same way and at the same time, but dipole moments, as shown in Figure 5.3, appear to have different phases. Therefore ϕ was allowed to vary in this analysis.

For comparison to experimental results, simulations of the Quantum Boltzmann equation were preformed using the same initial temperature and density that the experimental system was prepared in. The toy models used for the initial magnetizations are given by $M_x = \operatorname{sech}^2(z/\lambda_0)$, $M_y = \tanh(z/\lambda_0)\operatorname{sech}(z/\lambda_0)$, and $M_z = \tanh(z/\lambda_0)$. The dipole moment was calculated from the simulation results and fit with the damped sinusoid phenomenological model. The resulting data and fits are shown in 5.3b).

It is evident from the dipole moment plots that the lifetime in the case of larger domain wall width is much longer and the oscillations are slower in comparison to the small domain wall width case. Figure 5.4 summarizes the results, showing how damping rate, Γ, and oscillation frequency, f, change with domain wall width. Error bars on the experimental results are from fit uncertainties. The shaded regions show the results of the numerical simulations of the quantum Boltzmann equation. The area of the shaded regions encapsulate the measured shot-to-shot statistical fluctuations of temperature and density, both of which are around $\frac{5\%}{\sqrt{N}}$, where N is the number of data points used to fit each experimental dipole moment, which is roughly 36 points. The shaded area also includes the density calibration uncertainty due to systematic errors in measuring atomic density. Using measurements of condensate fraction, Reference [25] found our system could underestimate density by up to 10%.

Experimental and simulated results give reasonably good agreement. Certain parameters defining the initial spin preparation, such as transverse spin coherence, are not fully known and difficult to model so estimations of these parameters were used in simulations. The discrepancy between initial preparations may lead to slight disagreements between experimental and simulated data.

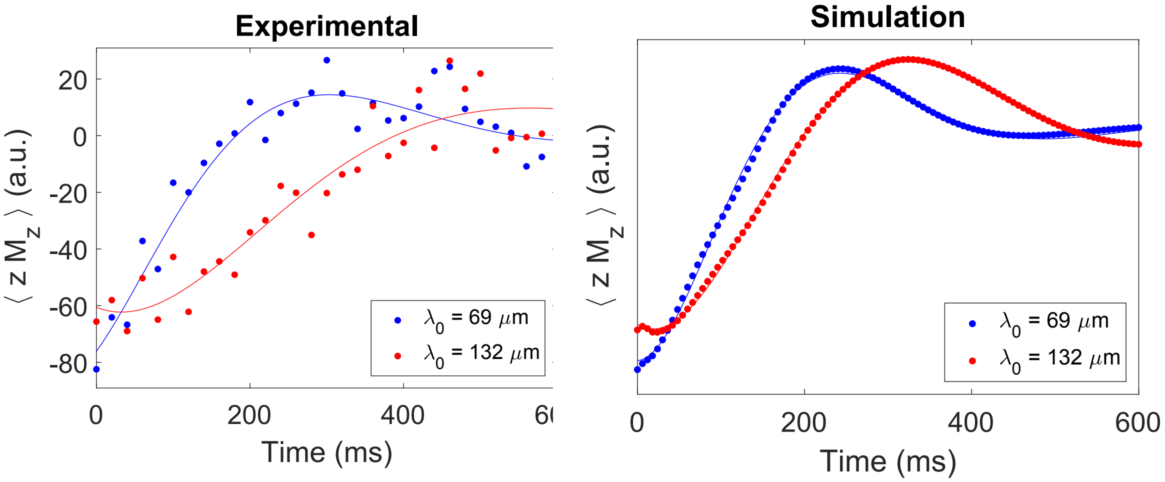

(a) (b)

Figure 5.3: a) Experimental and b) simulated time evolution of dipole moments of two-domain system with domain wall widths $\lambda_0 = 69\ \mu$m (blue) and $\lambda_0 = 132\ \mu$m (red). Dipole moments are fit to damped sinusoids.

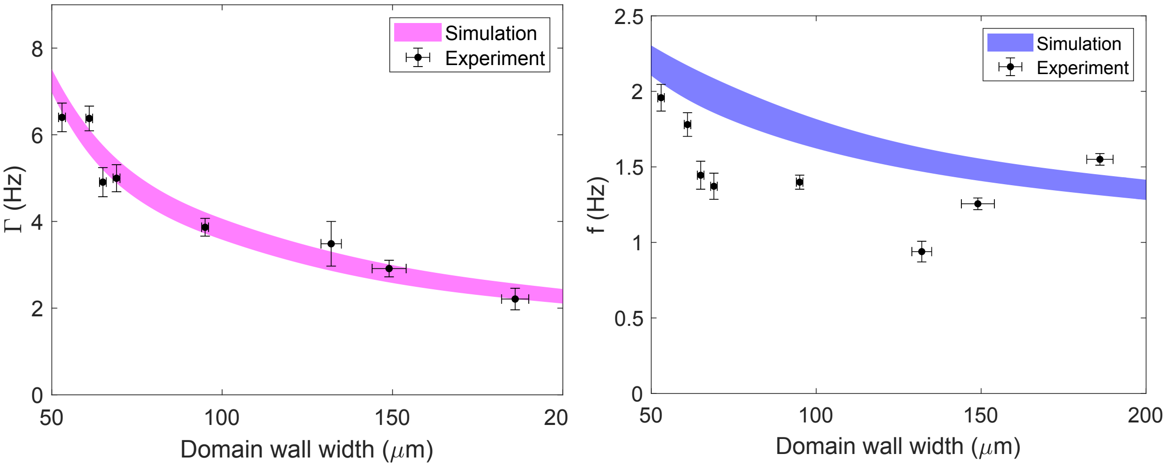

(a) (b)

Figure 5.4: The a) damping rate and b) oscillation frequency of the dipole moments of experimental and simulated data. Error bars of experimental data are fit uncertainties. The width of the simulation bands encapsulates statistical fluctuations and uncertainty in density calibrations.

Within large domain walls the spatial spin gradient across the domain wall is lower, such that an atom's spin is only slightly rotated during each ISRE collision, so an atom passing through the domain wall will follow and preserve the local spin; therefore the spin profile will remain roughly constant in time. Conversely, in a small domain wall the spatial spin gradient is higher, so during each ISRE collision the spins rotate further away from the mean spin. Since spins are changing faster, they are not adiabatically rotated through the domain wall. This results in larger changes to the spin profile over time, leading to a higher damping rate and faster oscillations in smaller domain wall configurations.

Our system operates between collisionless and hydrodynamic regimes, so analytic approximations of the quantum Boltmann equation in either of these limits do not accurately describe the dynamics. However, we can examine these limits, as well as the classical diffusion case, to give a sense of the bounds on the behaviour. In the case of classical diffusion, there would be no spin exchange collisions and thus we would expect spin oscillations to be at the trap frequency of 6.72 Hz. For the clouds studied here, we expect damping to be limited by the elastic collision rate, $\Gamma = \tau_{\text{elastic}}^{-1} = 84$ Hz. This gives an upper bound on both quantities. As the domain wall width approaches zero, we lose all ISRE interactions as there is no initial transverse spin present, thus we expect to increase towards the classical limits.

A damped oscillator can further be quantified by the Q-factor, $Q = \frac{2\pi f}{\Gamma}$, which describes how over or under-damped the oscillator is. Analytic predictions of oscillation and damping rates of a damped spin-wave oscillating about a steady-state solution in the hydrodynamic limit were made by Robert J. Ragan [36], which can be used to determine an expression for the Q-factor. The derivation of the expressions for damping and oscillation frequencies were based on analysis of the quantum Boltzmann equation with a positive linear differential potential acting on the spins. Using these analytic predictions, the Q-factor is found to be independent of any linear potential gradient, and is given by $Q = \sqrt{6}\mu M$. In the limit of a steady-state solution of zero, these results should be applicable to the damped spin-wave oscillation observed in a flat differential potential. For $\mu = 8$ and a fully polarized system with magnetization of $M = \left|\vec{M}(z,t)\right| = 1$, this expression predicts $Q \approx 20$. However magnetization decreases as time goes on due to decoherence and damping; Therefore we expect $Q = 20$ to be an upper bound on the Q-factor.

The Q-factor of experimental and numerical simulation results is shown in Figure 5.5. For all domain wall widths studied we find $Q > 1/2$, indicating slightly underdamped spin-wave oscillations. The analytic approximation of Q-factor is not explicitly dependent on domain wall width. The experimental results in Figure 5.5 also do not show a clear dependency on domain wall width, as most points are spread around $Q = 2$, with deviating points having large error bars. However, we do see an increasing trend in the simulation results. This is likely due to a faster loss of magnetization in configurations with a small domain wall width, leading to more quickly damped spin dynamics.

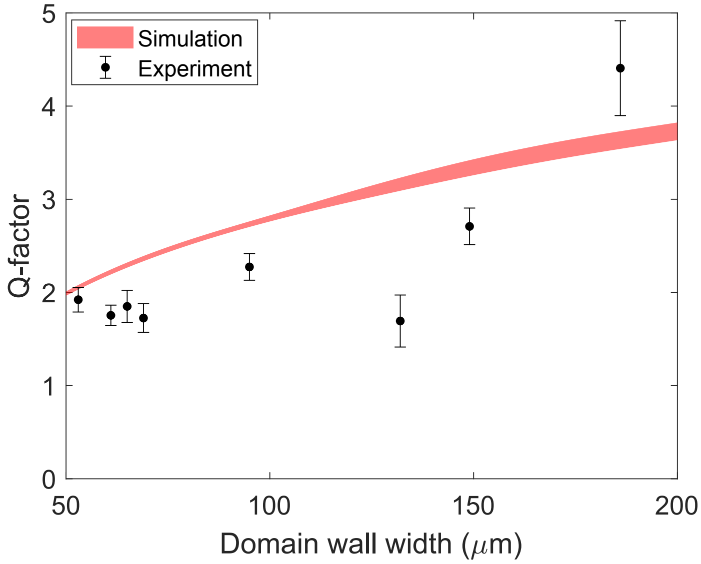

Figure 5.5: Q-factor of dipole moment fits calculated from the damping rates and oscillation frequencies shown in Figure 5.4

In summary, we observe that in a uniform differential potential, the spatial configuration of spins undergoes an underdamped spin-wave oscillation in time. Both the oscillation frequency and damping rate of longitudinal spin-waves decrease as the domain wall width increases. These effects can be attributed to smaller changes in the local spin orientation per ISRE collision in the domain wall for larger domain wall widths, therefore not significantly changing the spin profile over time.

5.2.2 Spin Dynamics in a Positive Linear Potential Gradient

Section 5.2.1 demonstrates that the strength of ISRE-generated spin currents are highly dependent on domain wall width. This raises the question: how will changing the initial domain wall width alter the spin diffusion dynamics in the presence of a differential potential? This question will be explored in this section.

To experimentally examine the spin dynamics behaviour, two-domain configurations of spin-states with various domain wall widths are prepared in the usual manner. Spins are allowed to evolve while a differential potential gradient of $U_{\text{diff}} = Gz$ is applied to the atomic cloud using the Stark shift laser reflected from the DMD. A gradient of $G = 46$ Hz/mm is used as the potential gradient size. Much larger gradients would show very fast decoherence, and much smaller gradients may not completely decay within the measured 600ms.

False colour plots of spin diffusion dynamics for various domain wall widths are shown in Figure 5.6a). Here we can see that for all domain wall widths, the domains stay evenly distributed and centred more closely around the zero axial position for around 200 to 300 ms, rather than exhibiting the large amplitude very slow oscillations observed in a flat differential potential. The corresponding dipole moments are shown in Figure 5.6b). The red dots show the experimentally measured dipole moments, while the blue dots are from numerically simulated data using similar initial conditions. Experimental dipole moment results lie reasonably closely to simulation results but appear to show slightly different transient oscillations. Discrepancies between results may be due to slight differences in intial conditions of the simulated data than in experiment conditions. Simulations use a toy model of initial magnetization that assumes a fully coherent transverse spin domain wall with amplitude of $\operatorname{sech}(z/\lambda)$ and phase of $\tanh(z/\lambda)$. These estimations were informed by older measurements of the initial transverse spin, but are likely outdated with newer DMD techniques that were previously described. The current experimental transverse spin may have a slightly lower amplitude or different phase profile, but was not measured. Future updated measurements of the initial transverse spin may be taken to ensure a close match between simulated and experimental initial conditions.

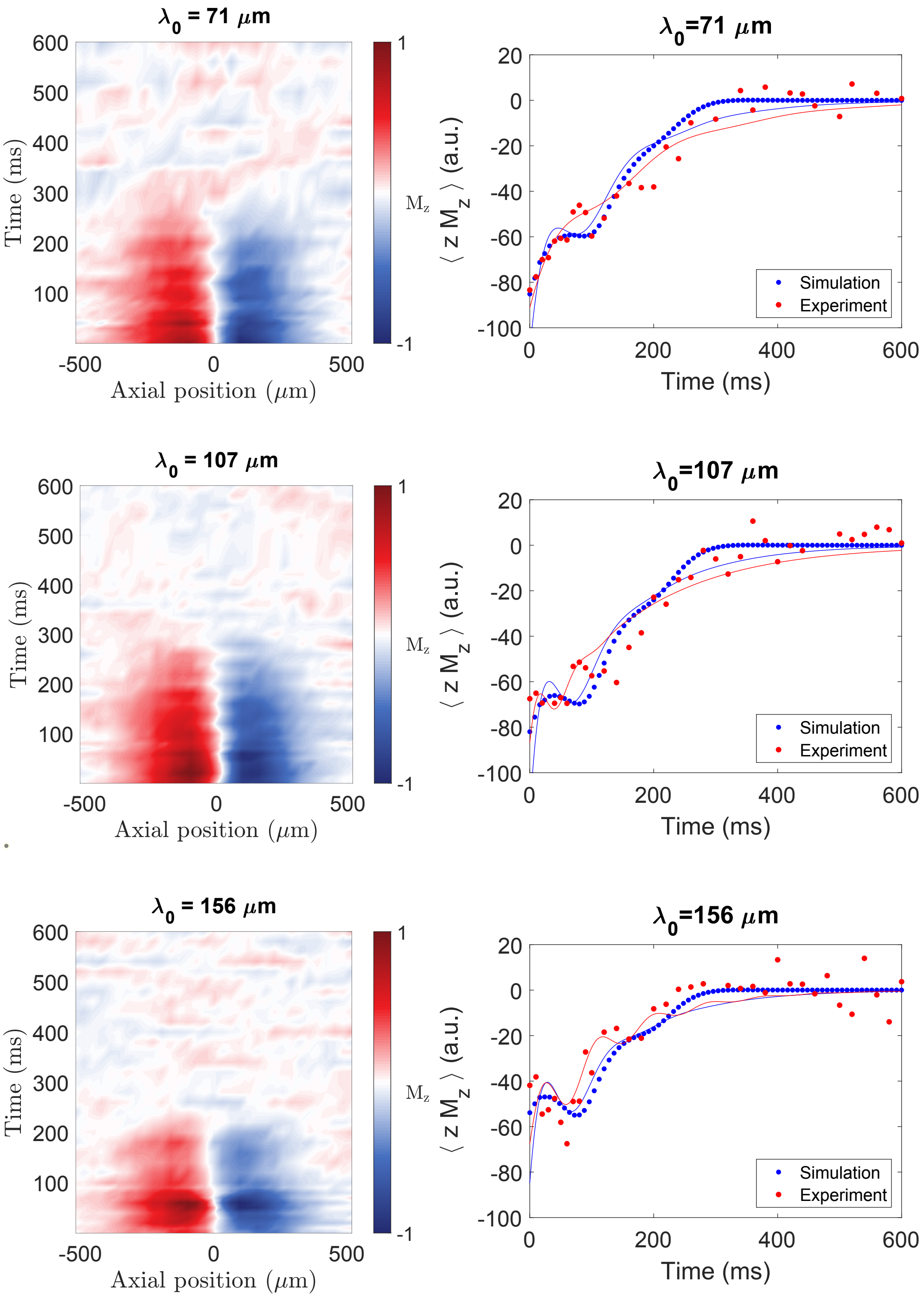

(a)

(b)

Figure 5.6: a) False colour plots and b) dipole moments of spin diffusion dynamics in a positive linear differential potential gradient of $G = 46$ Hz/mm for a two-domain preparation with domain wall width $\lambda_0 = 71$ μm, 107 μm, and 156 μm. In b) blue dots indicate simulated results. Red dots indicate experimental results. The corresponding lines are fits to a model of transient oscillations about a steady-state.

A phenomenological model used to describe this behaviour is given by $A\exp(-\Gamma_t t)\sin(2\pi f_t t+\phi)+B\exp(-\Gamma t)$, which describes a transient decaying oscillation about a steady-state solution. In the model, A and B are amplitudes, Γ is the steady-state damping rate, Γ_t, f_t, and ϕ are the transient damping rate, frequency, and phase respectively. Dipole moments of simulated and experimental data are fit to the phenomenological model, and the resulting fits are shown in Figure 5.6b) by the blue and red lines, respectively. Both fit amplitudes are constrained to be negative and the phase is fixed to π to minimize the number of variables required to be fit.

Fits indicate the approximation of an exponential steady-state decay does not accurately describe the behaviour. Further, the small transient oscillations make for difficulty in fitting, specifically in experimental results, where noise is present, resulting in poor agreement between simulation and experimental results. Due to the shortcomings of this model, the exact values extracted may not be completely accurate or reliable; however it is still useful to give a general idea of parameter behaviour at various domain wall widths.

The extracted parameters f_t, Γ_t, and Γ, for both simulation and experimental data are shown in Figure 5.7. Again, the shaded area of the simulation results represents the statistical fluctuations in temperature and density and systematic density uncertainty, while the error bars on experimental results are due to fit uncertainties. The transient oscillation frequencies extracted from the simulation and experimental data show very different behaviour, rendering our results inconclusive. Future work may be done to improve the phenomenological dipole moment fitting model to be able to draw conclusions on oscillation frequencies. However, trends can be seen in the transient and steady-state damping rates. Simulation results suggest that for some intermediate domain wall width ($\lambda_0 \sim 100$ μm), the transient damping rate reaches a maximum, though we are unable to conclude that the transient damping rate is maximized in experimental results, as error bars are large. Near this intermediate domain wall width, the steady-state damping rate appears to reach a minimum, indicating a maximum lifetime of the steady-state solution. However, differences in the steady-state damping rate between domain walls is fairly small since it is mainly driven by potential inhomogeneities. The potential inhomogeneities are approximately the same for all widths since the same differential potential gradient size is used and only slightly modified due to spin magnetization lost by transient decay. The changes in lifetime can also be seen in Figure 5.6, as the steady-state solution of the the domain wall initialized to 107 μm persists about 50 ms longer than both the smaller and larger domain wall systems.

This appears to give credence to hypotheses from R. Ragan [36], where an analysis of the quantum Boltzmann equation in the hydrodynamic regime with $G > 0$ was used to predict that there should exist some equilibrium domain wall width, λ_{eq}, such that when the domain wall width is initialized at the equilibrium width, the transients will be minimized and the lifetime of the two-domain spin system will be maximized. At the equilibrium domain wall width, we expect the spin rotation due to the ISRE to be exactly counter-balanced by the

Larmor precession of spins driven by potential gradients, leading to stable spin domains with minimal transients. We indeed see clear behaviour of extended lifetimes and quickly damped transients at an intermediate domain wall width, however the exact value of λ_{eq} for this particular system is unknown. Hydrodynamic predictions expect $\lambda \approx 125\ \mu$m, but since we are operating significantly away from the hydrodynamic regime this prediction may be unsatisfactory. Section 5.3 discusses a method of experimentally determining λ_{eq}.

Further, hydrodynamic analysis approximates the steady-state damping rate, frequency of transient, and transient damping rate at λ_{eq} as [36],

$$\Gamma \approx \left(\frac{G}{\mu^5 M^2} \omega_z^4 z_0 \tau^2 \right)^{1/3}, \tag{5.2}$$

$$f_t \approx \frac{\sqrt{6}}{2\pi} \left(\frac{4}{\pi^2} \frac{G^2}{\mu M} \omega_z^2 z_0^2 \tau \right)^{1/3}, \tag{5.3}$$

and

$$\Gamma_t \approx \frac{2\pi f_t}{\sqrt{6}\mu M} \tag{5.4}$$

respectively. For our experiment this predicts $\Gamma \approx 0.9$ Hz, $f_t \approx 5.7$ Hz, and $\Gamma_t \approx 1.9$ Hz. This approximation gives a reasonable estimation for the transient frequency, but significantly underestimates the damping rates. Outside of the hydrodynamic regime we expect damping rates to increase because atoms travel further between collisions, making it harder for them to maintain a local equilibrium. We can quantify the regime of the system by the Knudsen number, $\text{Kn} = \ell/\lambda_0$, where ℓ is the mean free path. The hydrodynamic regime has $\text{Kn} \ll 1$, while the collisionless regime has $\text{Kn} \gg 1$. The Knudsen number is dependent on density, and thus varies with position throughout the atomic cloud. Calculations in this thesis use a radially averaged density to determine the Knudsen number. In our system for inital domain wall widths ranging from 50 μm to 200 μm, Knudsen numbers lie between 1.9 and 0.5, indicating we are working in the crossover region.

We can also compare the Q-factor with the hydrodynamic prediction of $Q = \sqrt{6}\mu M \approx 20$. Figure 5.8 shows the Q-factor of simulated and experimental results. Error bars on the experimental results are very large due to the poor fitting of transient damping frequency in our dipole moment model. Specifically looking at the simulation results, we see that the values of the Q-factor are similar to what was seen in the case of a flat differential potential, lying within a range of about two to four. Again, results are much lower than the hydrodynamic prediction of $Q \approx 20$. The magnetization in the domain wall, $M = 1$, used in the calculation is an overestimate, and may be as low as $M \approx 0.7$, giving $Q \approx 14$. The magnetization may be lowered due to decoherence over the evolution time or phase inhomogeneities in initial preparations. According to simulation results, the Q-factor reaches a minimum near $\lambda_0 = 100\ \mu$m, the point where transients are minimized.

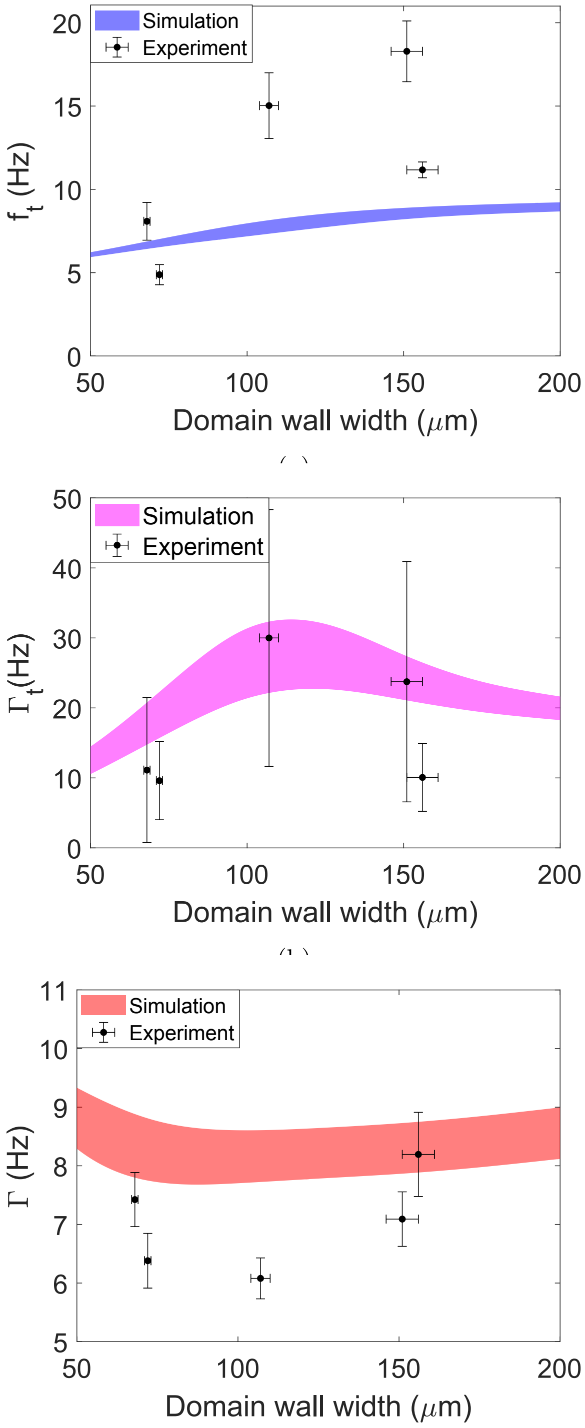

(c)

Figure 5.7: The a) transient oscillation frequency, b) transient damping rate, and c) steady-state damping rate of the dipole moments of experimental and simulated data. Error bars of experimental data are fit uncertainties. The width of the simulation bands encapsulate statistical fluctuations and uncertainty in density calibrations.

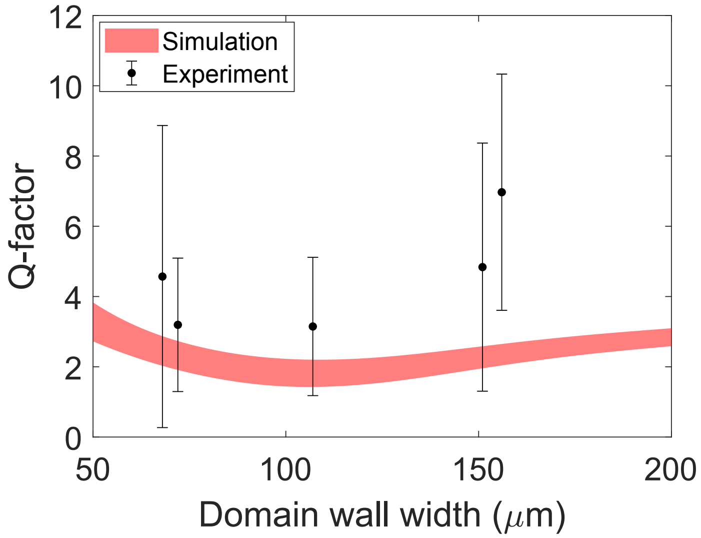

Figure 5.8: Q-factor of dipole moment fits calculated from the transient damping rates and oscillation frequencies shown in Figure 5.7

Overall, it was observed that in the presence of a positive linear differential potential, spin-wave dynamics show a damped transient oscillation about a steady-state decay. The spin waves were modelled as an exponentially damped sinusoidal transient around a decaying exponential steady-state solution to extract parameter values. This model does not fully capture the dynamics, but gives a reasonable estimation of parameter behaviours. Using this model we find that the transient damping rate reaches a maximum, while the steady-state damping rate reaches a minimum near some intermediate domain wall width. This result agrees with hypotheses that predict minimal short-lived transients near the equilibrium domain wall width, which lead to increased steady-state lifetimes as less magnetization is removed by the transients. The extracted experimental spin-wave parameters were determined through measurement in between the hydrodynamic and collisionless regimes and give poor agreement with analytic hydrodynamic predictions. Methods of determining equilibrium domain wall widths, and thus finding the spin preparation that will maximize spin-state lifetimes, is discussed in Section 5.3.

5.3 Determination of Equilibrium Domain Wall Widths

Section 5.2.2 discussed the effect a positive linear magnetic field gradient can have on stabilizing spin domains against spin wave oscillations and increasing lifetime. Based on analysis of the quantum Boltzmann equation in the hydrodynamic limit, Reference [17] predicts that for a stabilized two-domain trapped bosonic gas the relationship between equilibrium domain wall width and gradient size is given by

$$G = \frac{\omega_z}{z_0} \frac{1}{\mu M} \left(\frac{\pi/2}{1.1\lambda_{\text{eq}}/z_0} \right)^3 \omega_z \tau. \tag{5.5}$$

This equation was derived under the assumptions of slow diffusion ($\lambda_0 \ll z_0$), a collision rate that is large enough to ensure the spin current is in local equilibrium ($\omega_z \tau \ll 1$), and strong contributions from the ISRE ($\mu M \gg 1$). As discussed in Section 5.2.2, initializing the spin structure with $\lambda_0 = \lambda_{\text{eq}}$ for the particular gradient size used is expected to maximize the lifetime of the domains. The following research aims to determine the equilibrium domain wall width for a given gradient, based on the experimentally determined domain wall relaxation rate of various initial domain wall widths. This method follows work done in Reference [25].

Data is taken using a cloud of atoms with $n = 2.6 \times 10^{13}$ cm^{-3} and $T = 650$ nK. Atomic density is higher than previous sections for better comparison with hydrodynamic analytic approximations. The Knudsen number for domain wall widths, 50 μm $< \lambda_0 <$ 200 μm, at this density range from 1.0 to 0.25, indicating that we are still working in a crossover regime between hydrodynamic and collisionless, but closer to the the hydrodynamic regime than in previous sections. Spin profiles are measured for up to 100 ms. Measurements at each time step are repeated to get an average of three measurements to minimize errors due to temperature and density fluctuations. The domain wall size at each point in time is extracted using a fit to the model described in Equation 3.15.

For each gradient size used, the change in domain wall width relative to its initial width is mapped over time. Figure 5.9 shows the evolution in domain wall size over time for $G = 16$ Hz/mm. For a domain wall with $\lambda_0 = \lambda_{\text{eq}}$ there should be no changes in domain wall widths over short timescales. If $\lambda_0 > \lambda_{\text{eq}}$ the domain wall will shrink towards the equilibrium value. Conversely if $\lambda_0 < \lambda_{\text{eq}}$ the domain wall will expand towards the equilibrium value. The relaxation towards equilibrium width is approximately linear on short timescales, before significant damping occurs, which removes magnetization and changes the equilibrium width. For each initial domain wall width, the relaxation rate is extracted from the linear change in domain wall width over the short timescale where magnetization is roughly constant. Note that the domain wall width relaxing towards the equilibrium domain wall width is different than the relaxation of the steady-state solution towards an equilibrium spin mixture discussed in Section 5.2.2.

Applied potential gradients cause decoherence of transverse spin, also leading to loss of magnetization. As loss of magnetization occurs much faster for large gradients, relaxation rates of domain walls must be fit for smaller timescales. The fit timescale for each gradient size is chosen as the time in which the domain wall width appears to change linearly. Figure 5.10 shows the relaxation rate for various initial domain wall widths at different potential gradient strengths. Relaxation rates are limited by the rate of atomic collisions taking place near the edges of the domain wall; therefore as the initial domain wall width approaches the Gaussian width (187 μm) of the atomic cloud, fewer of these relaxation-driving collisions take place due to the lower density. Therefore for each gradient the trend between relaxation

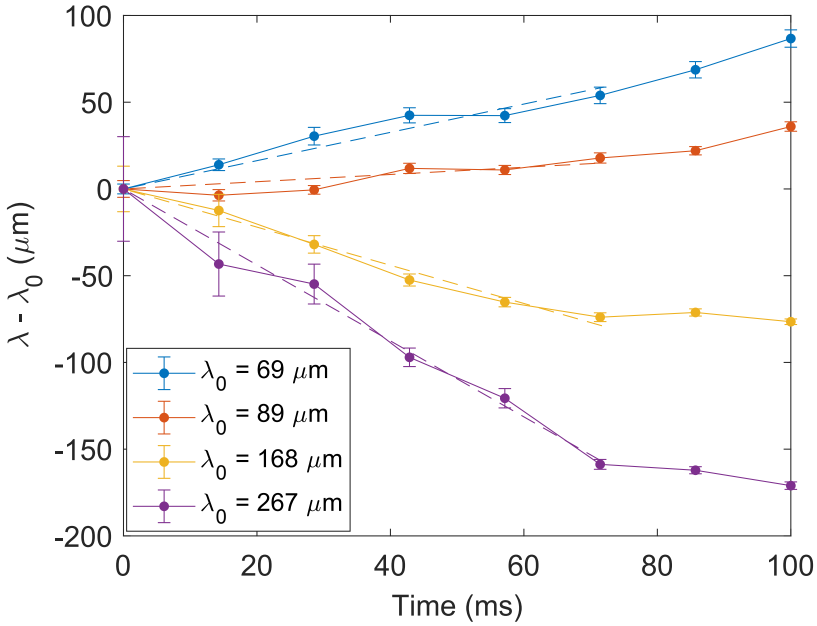

Figure 5.9: Domain wall relaxation in linear differential potential gradient of $G = 16$ Hz/mm. Relaxation is fit linearly over short timescales.

rates versus domain wall width is fit exponentially. The point where relaxation rate is equal to zero determines λ_{eq}.

The equilibrium domain wall widths are plotted alongside their corresponding stabilizing gradient in Figure 5.11. Error bars of the equilibrium domain wall width show uncertainty in the best fit of the exponential function. The blue region of Figure 5.11 shows the theoretical hydrodynamic predictions based on Equation 5.5. Here the shaded band represents a 5% uncertainty from the magnification of the imaging camera used to determine λ. We see somewhat good agreement between theoretical and experimental results for large domain wall widths, where Knudsen number is lower, indicating the system lies closer to the hydrodynamic regime. However, significant deviation is seen for small domain wall widths, which contradicts the assumption of $\lambda_0 \ll z_0$ used in derivation of Equation 5.5.

To show the effect of transients on the steady-state domains longer spin evolution time was studied for $G = 16$ Hz/mm at $\lambda_0 = \lambda_{\text{eq}} = 109$ μm and is depicted in Figure 5.12a). In this configuration stable spin domains are observed to 600 ms. In contrast, the dynamics shown in Figure 5.12b), with domain wall initialized at a value away from the equilibrium width ($\lambda_0 = 69$ μm), show longer transient lifetime and a slightly shorter lifetime of the spin domains, as predicted. Figure 5.12c) compares the dipole moments of a) and b).

In conclusion, this Section demonstrates a method of finding the equilibrium domain wall width for a given gradient magnitude. Initializing our spin-state profile at the equilibrium domain wall width stabilizes the domain wall on short timescales and elongates the

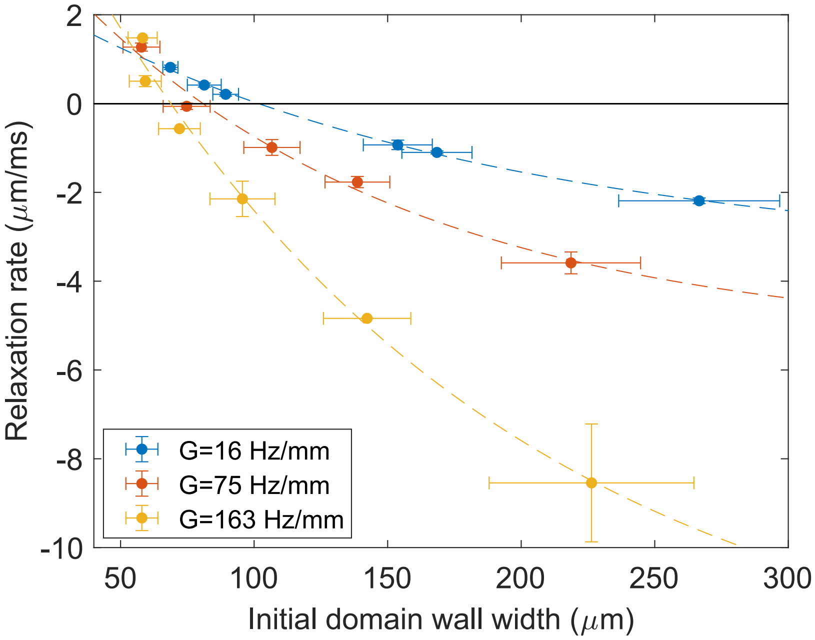

Figure 5.10: Domain wall relaxation rates for various initial domain wall widths, shown for three different linear potential gradients. Relaxation rates are fit exponentially. The intersection of the fitted lines and the black line indicates the equilibrium domain wall width, where no relaxation of the domain wall occurs at short times.

overall spin lifetimes. For small positive differential potential gradients, the experimentally determined equilibrium domain wall width agrees with hydrodynamic predictions.

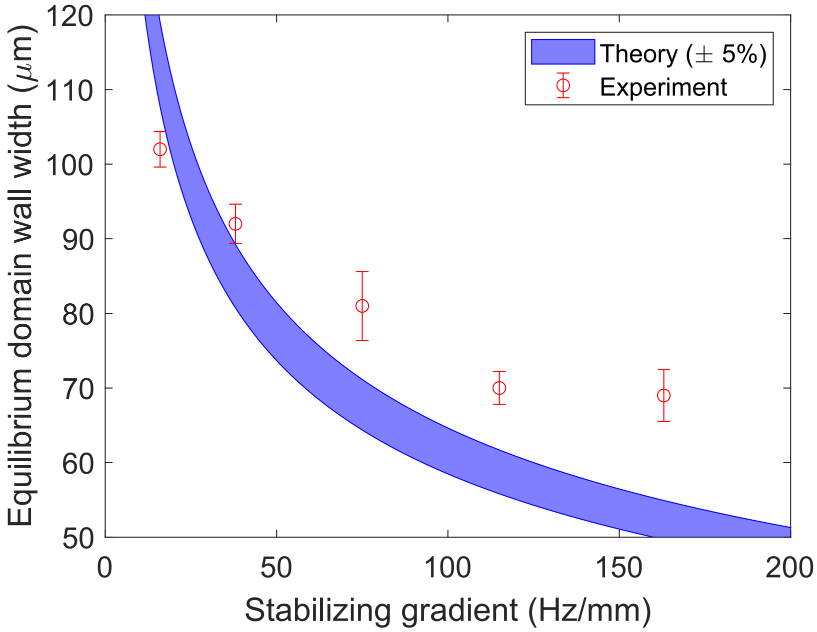

Figure 5.11: Equilibrium domain wall width corresponding to given linear differential potential gradients. Red markers correspond to experimentally determined widths, with error bars given by the uncertainty in exponential fit of the relaxation rate. The experimentally measured gradient sizes have point size error bars. The blue shaded region is the predicted relationship between gradient and equilibrium domain wall width in the hydrodynamic limit. The area of the shaded region is the experimental uncertainty in measuring domain wall widths.

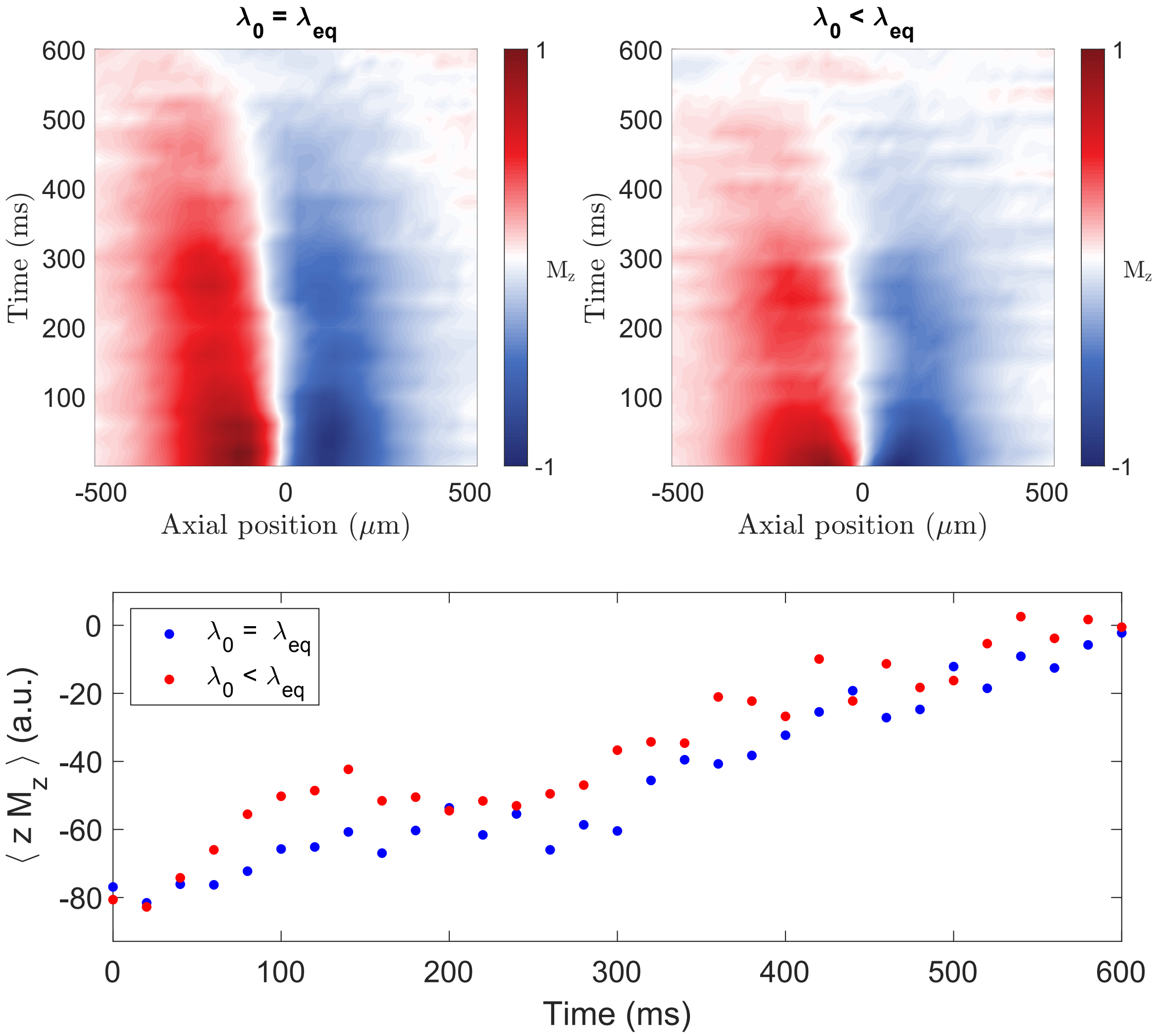

(c)

Figure 5.12: False colour plots of the spin diffusion of domains in G = 16 Hz/mm prepared with a) $\lambda_0 = \lambda_{\text{eq}} = 109\ \mu$m and b) $\lambda_0 = 69\ \mu\text{m} < \lambda_{\text{eq}}$. c) The dipole moments of a) and b). When prepared at the equilibrium domain wall width, domains show slightly longer lifetimes.

Chapter 6

Conclusion

In this thesis, we have examined the effects of domain wall width on the diffusion of a two-domain pseudo-spin configuration of a non-degenerate gas of Rb-87.

We began by discussing the relevant theoretical background of spin diffusion in Rb-87. Chapter 2 presented the fine and hyperfine energy level structure of Rb-87 and presented the states comprising the pseudo-spin doublet studied in this work. During spin collisions, the ISRE rotates spins about their mean spin. The spin diffusion in our experiment, including the effects of the ISRE, is described by the quantum Boltzmann equation.

In Chapter 3, the experimental procedure was outlined. First, methods of trapping and cooling were discussed. Next, we showed how spin states are prepared in arbitrary geometric configurations. Finally, procedures for image processing and extracting longitudinal spin measurements were described.

Differential potentials can have major effects on spin diffusion, so the control and measurement of them is very important. This was discussed in Chapter 4. Ramsey interferometry allows us to measure the differential potentials acting on the atomic cloud. A flat differential potential can be found at the cancellation spot, where the Zeeman shift and the mean-field shift approximately cancel. More complex differential potentials can be created using a Stark shift laser reflected from a DMD.

The results of our simulated and experimental studies were presented in Chapter 5. All work presented here looks at the effects of domain wall width on the spin diffusion of a non-degenerate bosonic atomic gas prepared in a two-domain configuration with a coherent domain wall. First, the spin diffusion dynamics in a uniform differential potential was investigated at domain wall widths from 50 μm to 200 μm. When prepared with larger domain wall widths, the resulting spin waves were shown to have slower oscillations and decay rates, due to the lowered transverse spin gradient across the domain wall leading to adiabatic following of local spin through ISRE collisions. Next, we examined spin diffusion dynamics in the presence of a linear differential potential gradient. In a linear differential potential gradient, the spin domains show a decaying steady state solution with transient oscillations about the steady state. Analysis of the dynamics at various domain wall widths show that at some intermediate domain wall width the decay rate of the transients reaches a maximum, while at a similar width the decay rate of the domains reach a minimum. This is inline with predictions. Results in uniform and linear potential gradients both deviated significantly from analytic approximations for the hydrodynamic limit. Lastly, equilibrium domain wall widths for various positive linear differential potential magnitudes were determined by analysis of domain wall relaxation rates on short timescales. The results show reasonable agreement with analytic predictions when domain wall widths are large. The results presented in this thesis expand our knowledge of the role ISRE plays in spin-wave dynamics and provide a better understanding of how one can optimally control spin diffusion by adjusting initial domain wall widths. This work is applicable to quantum technologies that require precise control and transport of spins.

In future experiments, the effects of domain wall width could be further explored at higher atomic density, for better comparison to hydrodynamic approximations. Analysis of the spin dynamics in linear differential potential gradients could be improved by determination of a better physically motivated model to fit dipole moments, or by studying smaller gradients ($G \sim 10$ Hz/mm), as the smaller transients produced would allow for better fits to the existing model. Also, our ability to extend spin domain lifetimes could be investigated further. For example, since magnetization decreases over time, one could apply stabilizing linear differential potential gradients that vary with time, according to the time-evolving magnetization, to continually stabilize domains and increase lifetimes. Further, experiments to understand the spin dynamics of different geometries can be considered. Studies of a 3-domain system are currently ongoing. These studies could also be expanded to higher n-domain configurations. There are a vast range of other unique spin geometries that have yet to be explored that may continue to advance our knowledge of quantum dynamics in atomic systems.

Bibliography

[1] Ramsey, N. F. History of Atomic Clocks. *Journal of Research of the National Bureau of Standards* **88**, 301–320 (1983).

[2] Chu, S. Laser trapping of neutral particles. *Scientific American* **266**, 71–76 (1992).

[3] Cohentannoudji, C. N. & Phillips, W. D. New Mechanisms for Laser Cooling. *Physics Today* **43**, 33 (1990).

[4] Anderson, M. H., Ensher, J. R., Matthews, M. R., Wieman, C. E. & Cornell, E. A. Observation of Bose-Einstein Condensation in a Dilute Atomic Vapor. *Science* **269**, 198–201 (1995).

[5] Mewes, M. O. *et al.* Bose-Einstein Condensation in a Tightly Confining dc Magnetic Trap. *Physical Review Letters* **77**, 416 (1996).

[6] Bose, S. N. Plancks gesetz und lichtquantenhypothese. *Zeitschrift für Physik* **26**, 178–181 (1924).

[7] Einstein, A. Quantentheorie des einatomigen idealen gases. *Sitzungsberichte der Preussischen Akademie der Wissenschaften, Physikalisch-mathematische Klasse* 261–267 (1924).

[8] Regal, C. A., Greiner, M. & Jin, D. S. Observation of Resonance Condensation of Fermionic Atom Pairs. *Physical Review Letters* **92**, 4 (2004).

[9] Singh, V. P. *et al.* Probing superfluidity of Bose-Einstein condensates via laser stirring. *Physical Review A* **93**, 023634 (2016).

[10] Byrnes, T., Wen, K. & Yamamoto, Y. Macroscopic quantum computation using Bose-Einstein condensates. *Physical Review A* **85**, 040306 (2012).

[11] Shaukat, M. I., Castro, E. V. & Terças, H. Quantum dark solitons as qubits in Bose-Einstein condensates. *Physical Review A* **95**, 053618 (2017).

[12] Nacher, P. J., Tastevin, G., Leduc, M., Crampton, S. B. & Laloe, F. Spin rotation effects and spin waves in gaseous 3He. *Journal de Physique Lettres* **45**, 441–448 (1984).

[13] McGuirk, J. M. *et al.* Spatial resolution of spin waves in an ultra-cold gas. *Physical Review Letters* **89**, 090402 (2002).

[14] Lhuillier, C. & Laloe, F. Transport properties in a spin polarized gas, I. *Journal de Physique* **43**, 197–224 (1982).

[15] Nikuni, T., Williams, J. E. & Clark, C. W. Linear spin waves in a trapped Bose gas. *Physical Review A* **66**, 10 (2002).

[16] Niroomand, D., Graham, S. D. & Mcguirk, J. M. Longitudinal spin diffusion in a nondegenerate trapped 87 Rb gas. *Physical Review A* **115**, 075302 (2015).

[17] Graham, S. D., Niroomand, D., Ragan, R. J. & McGuirk, J. M. Stable spin domains in a nondegenerate ultracold gas. *Physical Review A* **97**, 051603 (2018).

[18] Wolf, S. A. *et al.* Spintronics: A Spin-Based Electronics Vision for the Future. *Science* **294**, 1488–1495 (2001).

[19] Foot, C. *Atomic Physics* (Oxford University Press, 2005).

[20] Breit, G. & Rabi, I. I. Measurement of nuclear spin. *Physical Review* **38**, 2082–2083 (1931).

[21] Corney, A. *Atomic and laser spectroscopy* (Clarendon Press Oxford, 1978).

[22] Rabi, I. I. Space Quantization in a Gyrating Magnetic Field. *Physical Review* **51**, 652 (1937).

[23] Allen, L. & Eberly, J. *Optical Resonance and Two-level Atoms* (Dover Publications, 1978).

[24] Leggett, A. J. & Rice, M. J. Spin Echoes in Liquid He3 and Mixtures: A Predicted New Effect. *Physical Review Letters* **20**, 586 (1968).

[25] Graham, S. D. *Modifying spin diffusion in a nondegenerate ultracold gas*. Ph.D. thesis, Simon Fraser University (2019).

[26] Lewandowski, H. J. *Coherences and correlations in an ultracold Bose gas*. Ph.D. thesis, University of Colorado (1997).

[27] Metcalf, H. & Van der Straten, P. *Laser Cooling and Trapping* (Springer, 1999).

[28] Petrich, W., Anderson, M. H., Ensher, J. R. & Cornell, E. A. Behavior of atoms in a compressed magneto-optical trap. *Journal of the Optical Society of America B* **11**, 1332 (1994).

[29] Ketterle, W., Durfee, D. & Stamper-Kurn, D. Making, probing and understanding Bose-Einstein condensates. In *Proceedings of the International School on Physics "Enrico Fermi" 1998, Bose-Einstein Condensation in Atomic Gases*, 67–176 (IOS Press, 1999).

[30] DLP7000 data sheet. URL `https://www.ti.com/product/DLP7000`.

[31] Nelson, P. DLP®Technology for Spectroscopy. URL `https://www.ti.com/lit/wp/dlpa048a/dlpa048a.pdf?ts=1638650558428`.

[32] Zener, C. Non-adiabatic crossing of energy levels. *Proceedings of the Royal Society of London Series A* **137**, 696–702 (1932).

[33] Ramsey, N. F. A Molecular Beam Resonance Method with Separated Oscillating Fields. *Physical Review* **78**, 695 (1950).

[34] Harber, D. M., Lewandowski, H. J., Mcguirk, J. M. & Cornell, E. A. Effect of cold collisions on spin coherence and resonance shifts in a magnetically trapped ultra-cold gas. *Physical Review A* **66**, 053616 (2002).

[35] Grimm, R., Weidemüller, M. & Ovchinnikov, Y. B. Optical Dipole Traps for Neutral Atoms. In *Advances in atomic, molecular, and optical physics*, vol. 42, 95–170 (Elsevier, 2000).

[36] Ragan, R. Domain walls in 1d harmonic traps (2017). Private communication.